

BENEFIT FOA FY2015 - Solid State Magnetocaloric Air Conditioner - Final Report



Approved for public release.
Distribution is unlimited.

Ahmad Abuheiba
Ayyoub Momen
Mingkan Zhang
Joseph Rendall
Alexander Barcza
Hugo Vieyra

30-Sep-2020

DOCUMENT AVAILABILITY

Reports produced after January 1, 1996, are generally available free via US Department of Energy (DOE) SciTech Connect.

Website www.osti.gov

Reports produced before January 1, 1996, may be purchased by members of the public from the following source:

National Technical Information Service
5285 Port Royal Road
Springfield, VA 22161
Telephone 703-605-6000 (1-800-553-6847)
TDD 703-487-4639
Fax 703-605-6900
E-mail info@ntis.gov
Website <http://classic.ntis.gov/>

Reports are available to DOE employees, DOE contractors, Energy Technology Data Exchange representatives, and International Nuclear Information System representatives from the following source:

Office of Scientific and Technical Information
PO Box 62
Oak Ridge, TN 37831
Telephone 865-576-8401
Fax 865-576-5728
E-mail reports@osti.gov
Website <http://www.osti.gov/contact.html>

This report was prepared as an account of work sponsored by an agency of the United States Government. Neither the United States Government nor any agency thereof, nor any of their employees, makes any warranty, express or implied, or assumes any legal liability or responsibility for the accuracy, completeness, or usefulness of any information, apparatus, product, or process disclosed, or represents that its use would not infringe privately owned rights. Reference herein to any specific commercial product, process, or service by trade name, trademark, manufacturer, or otherwise, does not necessarily constitute or imply its endorsement, recommendation, or favoring by the United States Government or any agency thereof. The views and opinions of authors expressed herein do not necessarily state or reflect those of the United States Government or any agency thereof.

Energy and Transportation Science Division

BENEFIT FOA FY2015 - Solid State Magnetocaloric Air Conditioner - Final Report

Ahmad Abuheiba
Ayyoub Momen
Mingkan Zhang
Joseph Rendall
Alexander Barcza
Hugo Vieyra

Date Published:
November 2020

Prepared by
OAK RIDGE NATIONAL LABORATORY
Oak Ridge, TN 37831-6283
managed by
UT-BATTELLE, LLC
for the
US DEPARTMENT OF ENERGY
under contract DE-AC05-00OR22725

CONTENTS

CONTENTS.....	iii
1. INTRODUCTION	1
2. MCM MANUFACTURING.....	1
2.1 Producing MCM with surface roughness of 50 μm or less.....	2
2.2 High-throughput MCM manufacturing technoques.....	4
3. COMMERCIALIZATION	13
3.1 Competitive advantages of the smc ac	13
3.2 Market segment and size.....	14
3.3 Market potential	15
3.4 Steps toward successful market entry	16
4. MODELING AND PROTOTYPING.....	19
4.1 Solid Sate Model.....	19
4.2 Liquid-based AMR model	21
4.3 Prototype development	22
4.4 C-shaped prototype	22
4.5 Halbach prototype.....	25
5. References.....	28

LIST OF FIGURES

Figure 1. Schematic of the powder metallurgical production of La-Fe-Si alloys	2
Figure 2. Profile grinding machine to achieve smooth surface.....	2
Figure 3. Rods on an iron plate (left) and molybdenum plate (right)	3
Figure 4. Influence of support plate material during annealing treatment. A contact reaction between La-Fe-Si leads to reduced temperature change and shift of T_c (left), whereas iron plates do not show such a reaction (right).....	3
Figure 5. Surface testing device.....	4
Figure 6. Top-down cutting of parts with channels for solid-state heat transfer medium	5
Figure 7. Upper left: First LaFeMnSi tape casted out of a 10 wt.% binder slurry. A small plate was cut out. Upper right: the plate rolled down to a 1.2 mm bending radius. Lower image: sintered tape.	5
Figure 8. Form for the casting of $\sim 200\ \mu\text{m}$ tapes.....	6
Figure 9. Up: Tape after sintering. Bottom: Tape after hydrogenation.....	6
Figure 10. Negative form used to produce flexible silicone casting forms. The form exhibits features on its surface in order to cast tapes with defined surface patterns.	6
Figure 11. Thin foils of LaFeMnSi with surface patterns.....	7
Figure 12. Effect of shear rate on viscosity of the slurry. P is powder content of the slurry. $P_1 < P_2 < P_3 < P_4$	7
Figure 13. Viscosity as function of slurry powder content at shear rate typical of tape casting.....	8
Figure 14. Left: Tape caster. Right: hot rolling press used to produce thin tapes at VAC.	8
Figure 15. Left: P1 tapes cast with $h=0.5\ \text{mm}$ and different velocities. Right: The surface of the obtained tapes is not homogeneous.....	9
Figure 16. Left: P2 tapes cast with $h=0.5\ \text{mm}$ and different velocities. Right: The surface reveals a porous pattern after drying.....	9
Figure 17. Left: tapes cast with $h=0.5\ \text{mm}$ and different velocities. Right: Warping on the surface after drying is observed. Some crater-like defects are present due to trapped solvent bubbles	9
Figure 18. Left: tapes cast with $h=0.5\ \text{mm}$ and different velocities. Right: A smooth surface is obtained. However, some defects after drying are still present.	10
Figure 19. Thickness of the cast tapes as a function of cast velocity.....	10
Figure 20. The debinding furnace for the heat treatment of the cast tapes. Several components are explicitly indicated.....	11
Figure 21. The tapes after debinding and sintering. The results show that the tapes withstand the heat treatment with minor defects.....	12
Figure 22. Sintered and hydrogenated plates of a P3 slurry cast and pressed under inert gas. The magnetocaloric properties are comparable to the standard CALORIVAC-H values	13
Figure 23. Room AC share of residential space cooling market by region	14
Figure 24. Industry experts' assessment of the barriers impact and ease of overcoming	18
Figure 25. Representation of solid-state AMR [8].....	19
Figure 26. Response surface fitting coefficients [8].	20
Figure 27. Capacity and COP comparison of solid-state and liquid-based AMR [8].	20
Figure 28. Cooling capacity and COP for 16-layer liquid-based AMR as function of utilization for different frequencies [7].....	21
Figure 29. Effect of number of layers of liquid-based AMR on the cooling capacity and the COP [7].....	22

Figure 30. The C-shaped prototype showing the regenerators cam relative to the placement of the magnet. The cam profile is shown in the upper left corner. One magnet is shown in the lower right corner.....	23
Figure 31. Location of the pumping cam.....	23
Figure 32. Regenerator end caps. the thru holes are for mounting the regenerator tubes to the tray.....	24
Figure 33. Assembled prototype	24
Figure 34. External pumping system	25
Figure 35. The Halbach magnet array.....	26
Figure 36. Magnetic field strength at points 1 through 5 against rotation angle of the magnet array	26
Figure 37. The assembles prototype showing the regenerator tube sticking out of the left end of the Halbach array	27
Figure 38. No-load temperature span. Operating frequency is 0.6 Hz.....	27

LIST OF TABLES

Table 1. Surface roughness of annealed blocks	4
Table 2. Flatness and parallelism of the 5 mm face of the rods.....	4
Table 3. Flatness and parallelism of the 10 mm face of the rods.....	4
Table 4. Baseline costs used in the calculation of SMC AC payback period	15
Table 5. SMC AC payback period scenarios	15
Table 6. Time trend of maximum penetration after commercial viability	15
Table 7. SMC AC price point guidance	16
Table 8. Anticipated cost differences between SMC AC and conventional vapor compression RAC	16
Table 9. Parameter levels for design of experiment.....	19

1. INTRODUCTION

The active magnetic refrigeration (AMR) cycle holds great promise to reduce energy consumption of space cooling and heating. It is estimated that it could achieve up to 25% improvement in energy efficiency over conventional vapor compression systems. Prototypes have been built and demonstrated the working principles and energy benefits of the technology. These prototypes however were of low specific cooling power, defined as cooling power obtainable from unit mass of magnetocaloric materials (MCM). Specific cooling power is inversely proportional to the cost of the system. Therefore, for the magnetocaloric technology to be commercially viable, the specific cooling power must be increased. To increase the specific cooling power, for any MCM, the frequency of operation must increase. However, the maximum frequency that an AMR can operate at is limited by the residence time that is required to transfer heat in and out of the regenerator during the cold and hot blows. This time length is dependent on the thermal conductivity of the heat transfer medium. The higher the thermal conductivity of the heat transfer medium, the faster heat can be transferred between the medium and the MCM.

In 2014, ORNL filed a patent (granted in 2019) that describes a magnetocaloric refrigeration system that uses metallic mass as heat transfer medium [1]. Metals in general have two orders of magnitude higher thermal conductivity than liquids. This increase in thermal conductivity theoretically results in two orders of magnitude increase in the overall heat transfer rate between the heat transfer medium and the MCM. It is estimated that after accounting for all losses in an actual AMR system, the overall heat transfer coefficient between metallic medium and MCM will be 8 times higher than between liquid medium and MCM. This increase in heat transfer rate, would allow 5 to 10 times higher operational frequencies than with liquid heat transfer media. This means, 5 to 10 times the cooling power from the same MCM mass. The use of metallic heat transfer medium in an AMR imposes unconventional requirements on the form factor of the MCM in a regenerator. Typically, the MCM is packed into the regenerator in the form of spheres or irregular particles. With the use of metallic heat transfer medium, the MCM must be manufactured in sheets or blocks with low surface roughness. Regardless of the MCM manufacturing method, the magnetocaloric properties of the MCM must be retained.

In 2015, project was kicked off to develop the first solid-state magnetic air conditioner. The project had three main objectives:

1. Develop MCM manufacturing method
2. Develop commercialization plan
3. Design, optimize and build proof-of-concept prototype

This report summarizes the work that was performed over the course of the projects in each of three thrusts above. Each objective will be reported on in a separate section in the order in which the objectives are listed above.

2. MCM MANUFACTURING

The MCM manufacturing tasks aimed to develop method to manufacture MCM at scale in shapes and with surface quality that meets the requirements of the SMC AC. The tasks first focused on producing the MCM in blocks with surface roughness of 50 μm or less. After achieving that goal, the focus shifted to ways to manufacture MCM sheets at high throughput. The work of this task was mainly performed in the laboratories of Vacuumschmelze GmbH & Co. KG (VAC) in Germany.

2.1 PRODUCING MCM WITH SURFACE ROUGHNESS OF 50 μm OR LESS

LaFeCoSi was produced by the powder metallurgy route (see Figure 1). Master alloys were cast, crushed into a coarse powder ($< 1\text{ mm}$) and milled in a jet mill to a fine powder ($< 10\text{ }\mu\text{m}$). The desired composition was achieved by blending of fine powder batches. These blends were compacted in an isostatic press into rectangular blocks ($\sim 3\text{ kg}$ per block) and sintered under vacuum at about 1100°C to reach full density.

After sintering, the material cannot be machined directly by conventional machining methods. The reason is that at the magnetic phase transition temperature of the alloy, e.g. 25°C the material undergoes a negative thermal expansion, i.e. it shrinks by about 1% in volume.

If a specimen is machined at e.g. 20°C , the surface of the material heats up above its phase transition temperature due to friction with the tool (e.g blade, grinding tool, drill, etc.). It will therefore undergo a magnetic phase transition and shrink by 1%. The bulk of the material is still at 20°C and about 1% larger than the surface. This leads to huge stresses and eventually cracks in the material.

In order to machine the alloy further, it has to undergo thermal treatment. This treatment is carried out at around 800°C . This temperature treatment is necessary to induce a material transformation on the microscopic scale. The magnetocaloric La-Fe-Co-Si phase decomposes into α -iron and La-rich phases. Such a material has no magnetocaloric effect and hence no magnetic phase transition around room temperature (other than the one of α -iron which takes place at 768°C). The decomposed material can be machined by methods used for example to produce permanent magnets.

Subsequently rectangular rods with a dimension of $10 \times 5 \times 150\text{ mm}$ were cut from the starting material by wire electric discharge machining (EDM). The type of machines used lead to a surface roughness of typically $\sim 20\text{ }\mu\text{m}$, which was not considered sufficient for the purpose of this project. Technically this surface roughness would meet the criterion of MS1, however individual surface features of over $50\text{ }\mu\text{m}$ would risk the smooth movement of a solid heat transfer rod across the magnetocaloric material.

In order to reduce the surface roughness to a level acceptable to build a fully solid-state prototype, a grinding operation was required. The rods produced by wire-EDM could be used for the grinding tests. These tests were carried out at a profile-grinding machine using diamond-grinding wheels. The wheel speed, water flow, and feed rate were adjusted to give a smooth surface. After grinding, the rods were cleaned in an ultra-sonic bath using mild cleaning agent.

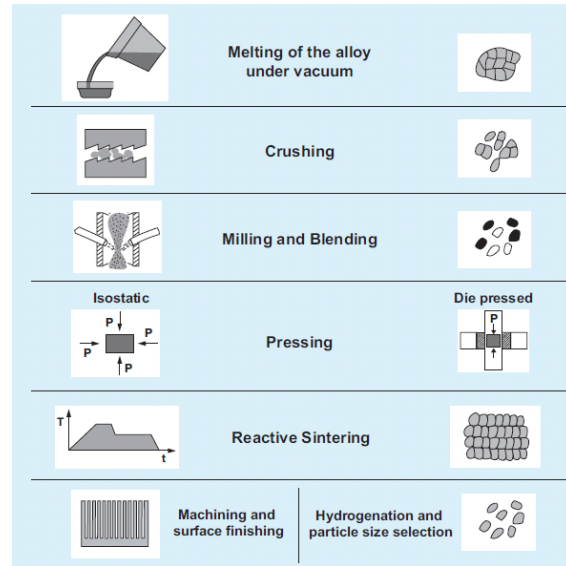


Figure 1. Schematic of the powder metallurgical production of La-Fe-Si alloys



Figure 2. Profile grinding machine to achieve smooth surface

In order to reinstate the magnetocaloric properties in the material a second heat treatment after machining had to be conducted. At a temperature of about 1050°C the two phases, α -Fe and La-rich phase, recombine to yield the desired La(Fe,Si)_{13} magnetocaloric phase. This is a critical step in the process chain since it is carried out at high temperature where the material becomes softer and is prone to deformation. In a first test the rods were annealed on a flat iron plate (see Figure 3 left). After heat treatment the surface of the rods was unchanged but the rods appeared bent by a simple optical inspection on a flat surface. In another test the rods were put on a flat molybdenum plate polished to a mirror finish (see Figure 3 right). After heat treatment, the rods were partly sintered onto the molybdenum plate. This means that there is a reaction between La-Fe-Si and the Mo-plate. A measurement of the magnetocaloric properties of a piece of the rod that was close to the affected area showed that the properties of the annealed material were worse than the starting material (Figure 4 left). On the other hand the material annealed on an iron plate showed no significant change of properties compared to the state before machining and annealing (see Figure 4 (right)). A simple measure to combine both features is to use the flat molybdenum plate and cover it with a thin iron foil. The foil will act as a separation layer between the Mo and the La-Fe-Si while not influencing the mechanical properties of the rods.

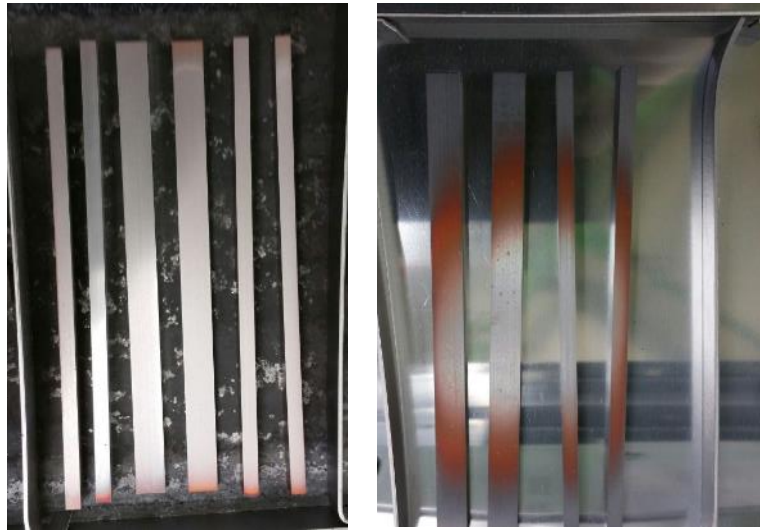


Figure 3. Rods on an iron plate (left) and molybdenum plate (right)

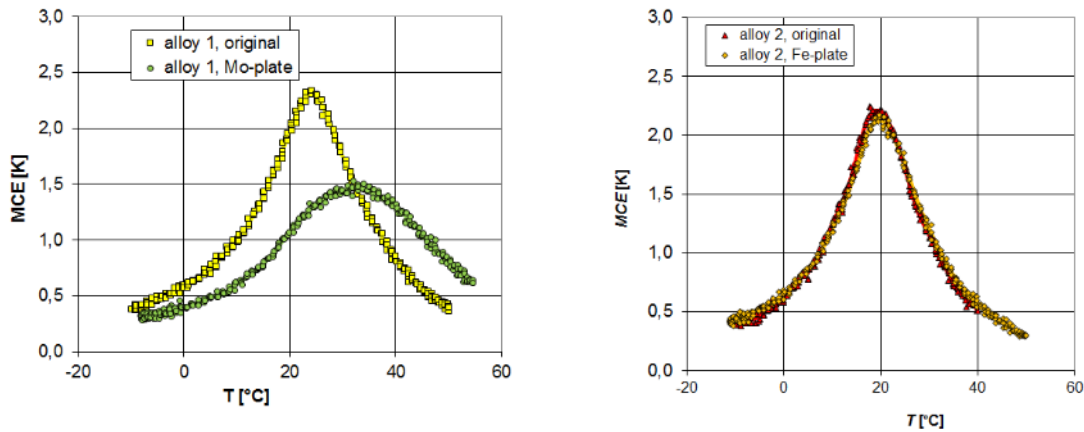


Figure 4. Influence of support plate material during annealing treatment. A contact reaction between La-Fe-Si leads to reduced temperature change and shift of T_C (left), whereas iron plates do not show such a reaction (right).

After annealing on the Mo-plate the rods were tested with a surface measuring device (see Figure 5). The surface roughness, parallelism, and flatness were each tested along the whole 150 mm length. Parallelism and flatness were measured on the 5 mm wide face and on the 10 mm wide face. Roughness was measured on the same faces of the two rods. The results are summarized in Table 1, Table 2 and Table 3. From Table 1 it can be seen that the surface roughness is very low with all values below 6 μm along the 150 mm length of the parts. This result shows that it is possible to manufacture the required quality of parts using a grinding operation.

The flatness of the rods over 150 mm after annealing is typically less than 0.05 mm with only one value being slightly larger (see Table 2 and Table 3). Despite the fact that flatness was not part of the original requirements, it still poses an important parameter. For a solid-state solution, it is required to build regenerator structures out of flat parts (plates, rod, etc.). Any bowing, tilt or curvature along the length of the regenerators will lead to a larger gap between the magnetocaloric material and the metallic heat exchange rod. This leads to a reduction in heat transfer coefficient, increase in friction, and in general a less efficient machine. The parallelism of the rods is generally larger than 0.05 mm. This value has to be improved for reliable operation for the prototype. It has to be said however that the regenerator will consist out of several parts assembled one after the other along the length of the regenerator. Each part will consist of one alloy and it is therefore only important to guarantee the mechanical properties along the length of one part. It is expected that this length will range from 10 – 30 mm depending on the detailed design of the device.



Figure 5. Surface testing device

Table 1. Surface roughness of annealed blocks

	R_a (μm)	R_z (μm)	R_{max} (μm)
Rod 1, surface 1	0,313	3,644	4,649
Rod 1, surface 2	0,285	3,081	5,084
Rod 2, surface 1	0,411	3,244	4,478
Rod 2, surface 2	0,321	3,570	5,366

Table 2. Flatness and parallelism of the 5 mm face of the rods

	Flatness (mm)	Parallelism (mm)
Rod 1	0,052	0,099
Rod 2	0,013	0,077

Table 3. Flatness and parallelism of the 10 mm face of the rods

	Flatness (mm)	Parallelism (mm)
Rod 1	0,004	0,243
Rod 2	0,015	0,202

2.2 HIGH-THROUGHPUT MCM MANUFACTURING TECHNOQUES

Top-down cutting techniques (subtractive manufacturing) have been used to fabricate parallel plate heat exchangers of LaFeCoSi alloys in the past. Such structures offer flexibility regarding the design since techniques such as wire EDM can be used. That method does not require any special tools and almost all shapes can be cut. For conventional fluid based magnetocaloric regenerators parallel plate heat exchangers offer the advantage of low pressure drop due to their regular shape of flow channels.

In this project this technique has been used to cut similar structures of non-hydrogenated LaFeMnSi alloys. The requirements for a fully solid-state technology are different. Since the heat capacity of the

metal rods or plates that should act as heat transfer medium is lower compare to water the ratio between magnetocaloric material and heat transfer medium should be different. Figure 6 shows an example of a LaFeMnSi alloy having a ratio of material to channel of about 1:3.

Two main disadvantages of wire EDM still remain. First, the required surface roughness of less than 50 μm cannot be guaranteed with the machines used¹. Second, the yield and productivity are low and not sustainable for commercialization. Despite these two risks, parts similar to the ones shown in Figure 6 could still be used to test one of the central hypotheses of this project. That is the question whether it is possible to use metal rods or plates as heat transfer medium and build a fully solid state active magnetocaloric regenerator.



Figure 6. Top-down cutting of parts with channels for solid-state heat transfer medium

The disadvantages of top-down techniques mentioned above mandate research in bottom-up methods shaping techniques for LaFeMnSi. One of such manufacturing processes developed is the tape-casting of LaFeMnSi. Tape casting would allow the production of thin foils of magnetocaloric material with a thickness below 200 μm . Furthermore, such films could be used as building blocks for three dimensional stacked structures.

As a first step, a slurry containing the magnetocaloric precursor powder was developed aiming for a proof-of-principle milestone. Apart from the precursor alloy, the slurry formulation contains a binder and a solvent. The binder provides the green tape not only with mechanical stability but also with some flexibility for the tape production and handling. The solvent is essential to dissolve the binder and significantly affects the drying of the tapes. All slurry components must be compatible with LaFeMnSi, that is, they should be easily burnt out prior to sintering and should leave no impurities. A compatible binder system for LaFeMnSi fulfilling these conditions was already known prior to the start of the project. The suitability of the binder with respect to tape casting was entirely in the open.

Polypropylene carbonate (PPC) leaves very low impurities after debinding and has a minimal impact on the magnetocaloric properties. The polymer exhibits a glass transition around 30-40°C, making it flexible under these conditions. First tests showed that 5 to 10 wt.% PPC give usually enough strength and add flexibility to green tapes. Methyl-ethyl-ketone was used as solvent in different concentrations.

First tapes were produced by manually spreading the slurry on silicone-coated baking paper. The test was done in ambient air. Figure 7 shows a tape with 10 wt.% PPC and with a mean thickness of 320 μm . The tape can be easily cut and rolled down to a bending radius of 1.2 mm. The cut plate was debinded and sintered to yield a dense tape with good flatness.

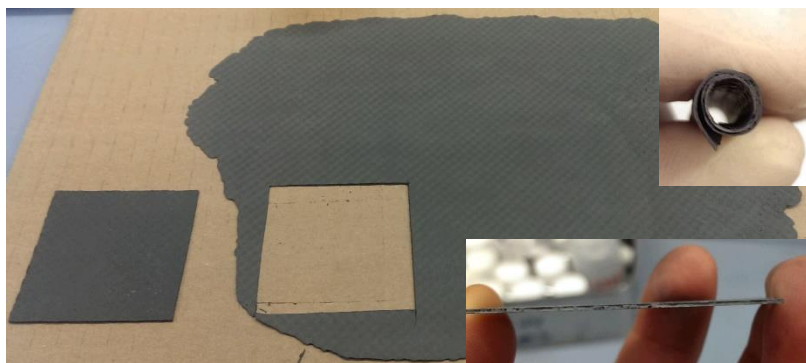


Figure 7. Upper left: First LaFeMnSi tape casted out of a 10 wt.% binder slurry. A small plate was cut out. Upper right: the plate rolled down to a 1.2 mm bending radius. Lower image: sintered tape.

The formulation of the slurry was optimized for thinner foils. Since the slurry does not contain a dispersant, a fast-drying slurry was preferred. In order to cast more homogeneous tapes, forms made of silicone-coated adhesive tape, like the one in Figure 8 were prepared. The forms were about 40 mm wide and 150 mm long and with a depth of

¹ There exist high-end wire EDM machines that can achieve better surface roughness but cutting speed is even lower and production costs are assumed to be significantly higher.

around 0.2 mm. Aiming for lower impurity levels, the content of PPC in the slurry was reduced. This slurry was manually spread over the form and dried in air for a couple of minutes. The resulting green tape shows good strength and retains some flexibility.

The tape was debinded and sintered. A very positive result was obtained since the form of the tape was retained after thermal treatment (Figure 9). The thin foil showed a thickness around 160 μm with a density of 7 g/cm^3 which is close to the theoretical density of 7.2 g/cm^3 . This cast foil can be regarded as a proof-of-principle for the casting of thin LaFeMnSi foils under 200 μm . In a further step this tape was hydrogenated resulting in a foil with a visible crack. This is a promising first result but requires further optimization of the hydrogenation treatment.

Dark areas on the edge of the foil were observed. These develop most probably due to oxygen contamination. Since the thermal treatment was performed entirely in a cold-wall furnace, contamination due to the decomposition products of the binder cannot be ruled out. For a proper debinding treatment a dedicated debinding furnace is needed. A dedicated debinding furnace has been purchased and installed in September 2017.

The promising results of the first trials resulted in an effort to improve the shape of the tapes. A negative mask for the preparation of more precise casting forms has been designed. Using this negative form, positive forms of flexible silicone were created (Figure 10).

Such forms allow the production of tapes with structure on their surface. The surface pattern would help stacking foils together while maintaining a gap between them. Tapes with different thickness $\leq 200 \mu\text{m}$ are being currently produced under inert conditions in order to further minimize oxygen contamination. Figure 11 presents some of the already casted foils using this technique.

Next step was to develop the slurry formulation for different tape casting conditions and optimize the debinding and sintering processes to minimize deformation to the finished parts. A slurry is a mixture of material powder and binder that is fed to tape caster. VAC investigated the rheology of different slurries containing different amounts of CALORIVAC powder. Figure 12 shows the effect of shear rate on viscosity of the slurry for different powder contents. The viscosity of the slurry increases as the powder content increases.



Figure 8. Form for the casting of $\sim 200 \mu\text{m}$ tapes



Figure 9. Up: Tape after sintering. Bottom: Tape after hydrogenation.

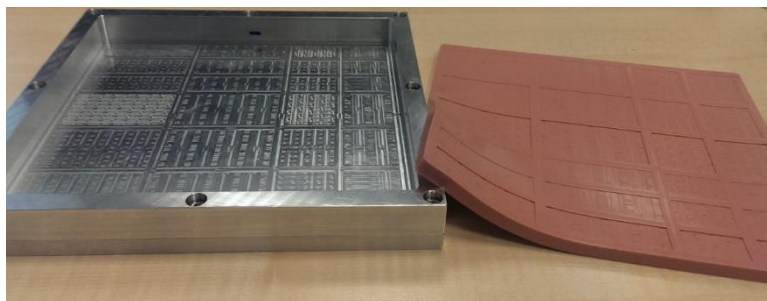


Figure 10. Negative form used to produce flexible silicone casting forms. The form exhibits features on its surface in order to cast tapes with defined surface patterns.

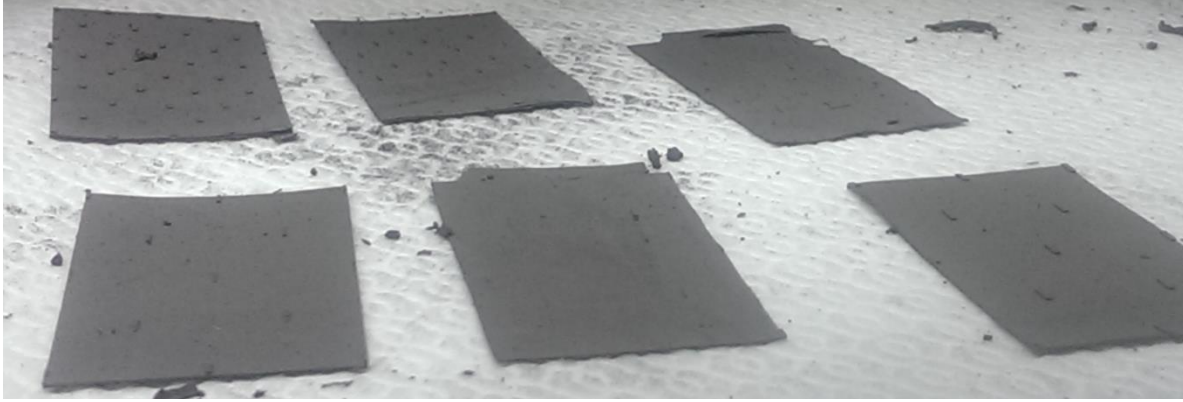


Figure 11. Thin foils of LaFeMnSi with surface patterns

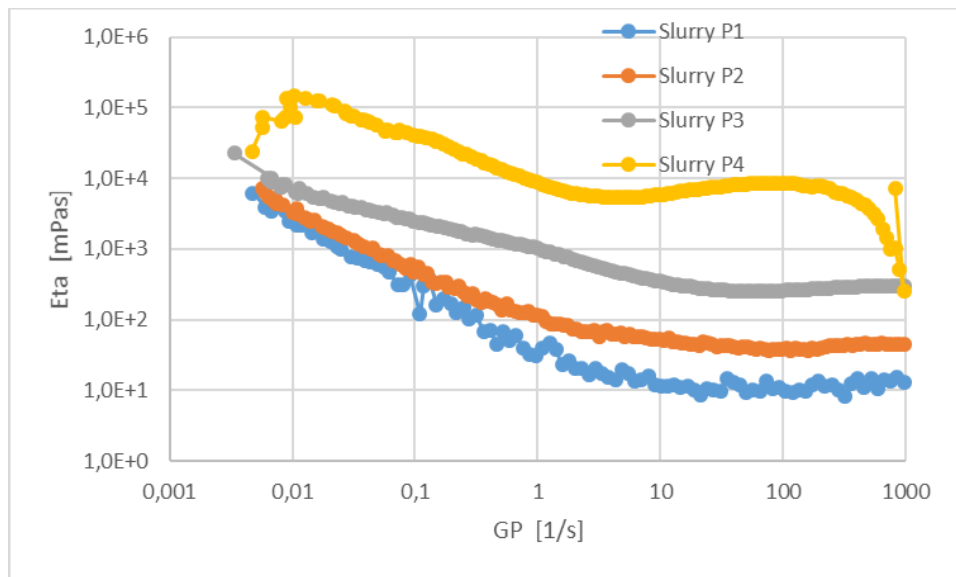


Figure 12. Effect of shear rate on viscosity of the slurry. P is powder content of the slurry. $P1 < P2 < P3 < P4$

Figure 13 shows the viscosity of the same four slurries at shear rate of 1/s, typical rate for tape casting. The figure shows that viscosity increases exponentially with the increase of the powder content.

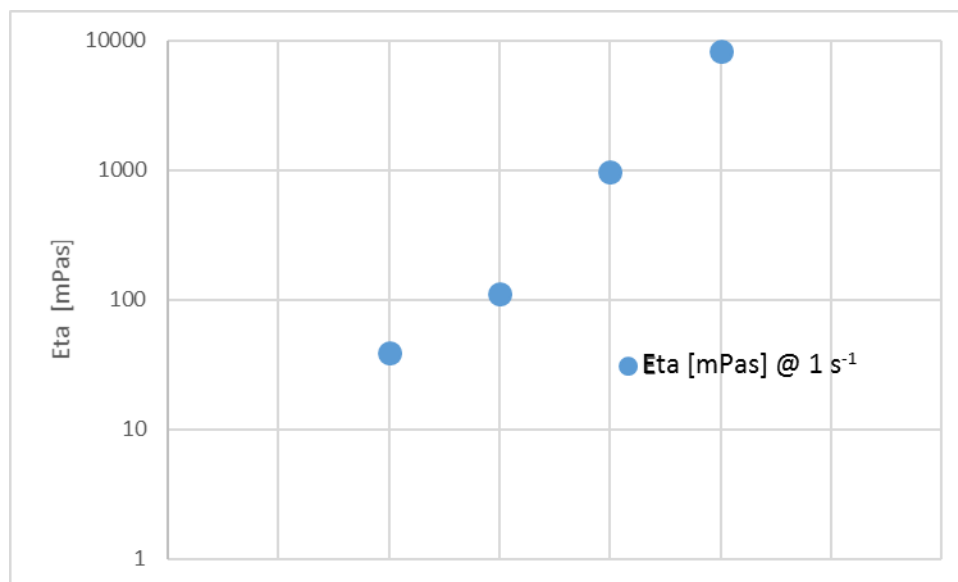


Figure 13. Viscosity as function of slurry powder content at shear rate typical of tape casting

The four slurries were cast into thin films using a tape caster. VAC purchased a lab-scale tape casting machine and a hot rolling press (Figure 14) for the development of thin foils within this project. The devices were carefully calibrated before they were put into operation.

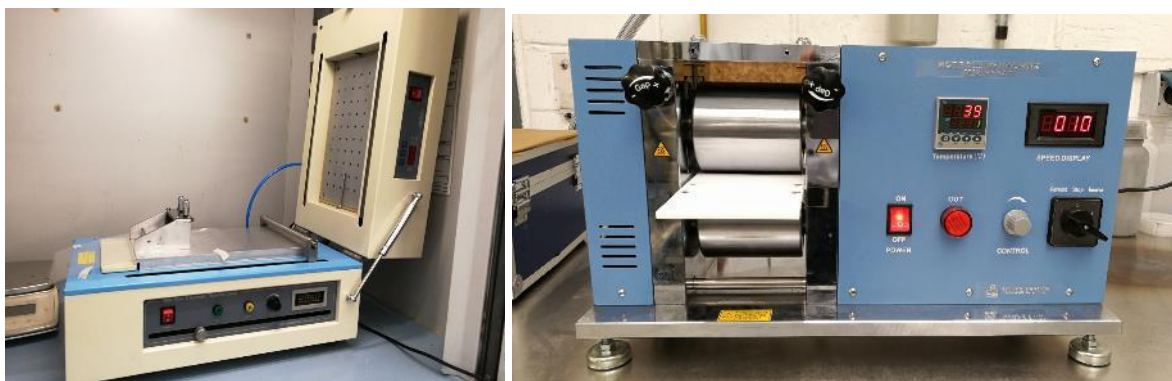


Figure 14. Left: Tape caster. Right: hot rolling press used to produce thin tapes at VAC.

The slurries were cast in air under normal temperature and pressure conditions. Two variables can be freely set for the process: the height of the doctor blade “h”, and the casting velocity “v”. For the tests with different powder concentrations the height of the doctor blade was set to 0.5 mm. The velocity was varied between 10 and 40 mm/s. Figure 15 shows the produced tapes with the P1 slurry. Being this the lowest powder concentration, the amount of solvent used was very high. This led to an inhomogeneous drying process and separation of slurry components. As shown, the surface of the tapes was not smooth and contained residues of the binder.

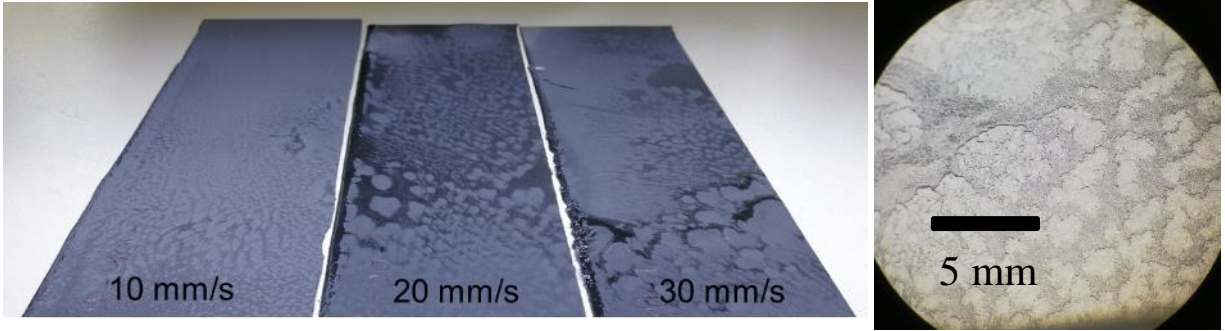


Figure 15. Left: P1 tapes cast with $h=0.5$ mm and different velocities. Right: The surface of the obtained tapes is not homogeneous.

Figure 16 shows the results for the P2 slurry. In this case the drying process led to a homogeneous and smooth surface. However, a closer look at the surface reveals a pattern with high porosity.

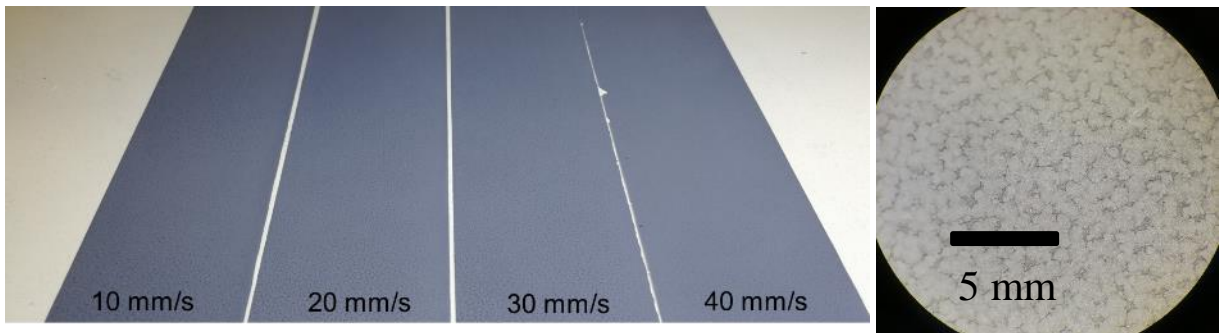


Figure 16. Left: P2 tapes cast with $h=0.5$ mm and different velocities. Right: The surface reveals a porous pattern after drying

The P3 tapes are shown in Figure 17. A homogeneous surface is observed with some warping. Other crater-like defects are present because of the drying process (trapped solvent bubbles).

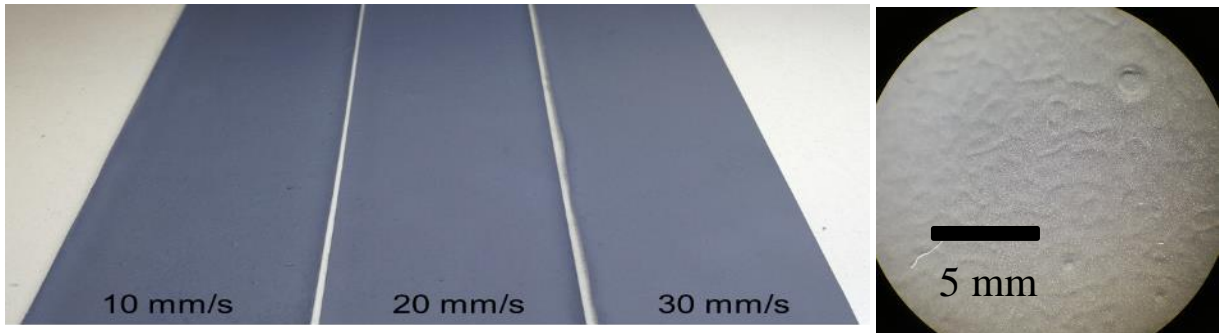


Figure 17. Left: tapes cast with $h=0.5$ mm and different velocities. Right: Warping on the surface after drying is observed. Some crater-like defects are present due to trapped solvent bubbles

Figure 18 shows the tapes produced with the P4 slurry. Very smooth surfaces are in general obtained. However, some defects are still present due to the drying process. As in P3, solvent bubbles are trapped during the drying process leading to those defects. Since the powder concentration in P4 is the highest, the solvent content is drastically reduced. This makes the P4 slurry difficult to process due to its high viscosity and the fast-drying process.

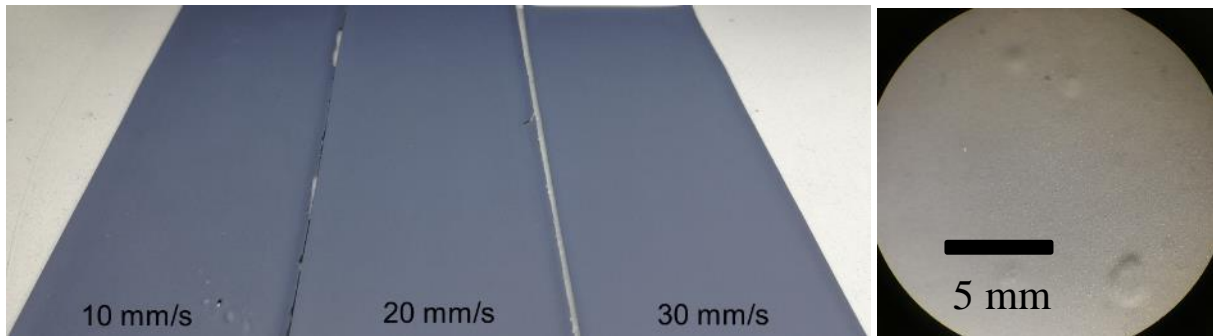


Figure 18. Left: tapes cast with $h=0.5$ mm and different velocities. Right: A smooth surface is obtained. However, some defects after drying are still present.

Figure 19 shows the dependence of the tape thickness on the velocity of casting. In general, the faster the tapes are produced, the thinner they become after drying. With increasing powder content, thinner foils can be produced at a constant velocity. For a doctor blade height of 0.5 mm it is possible to produce green tapes with thickness between 0.25 and 0.4 mm by varying the formulation of the slurry and the velocity of casting.

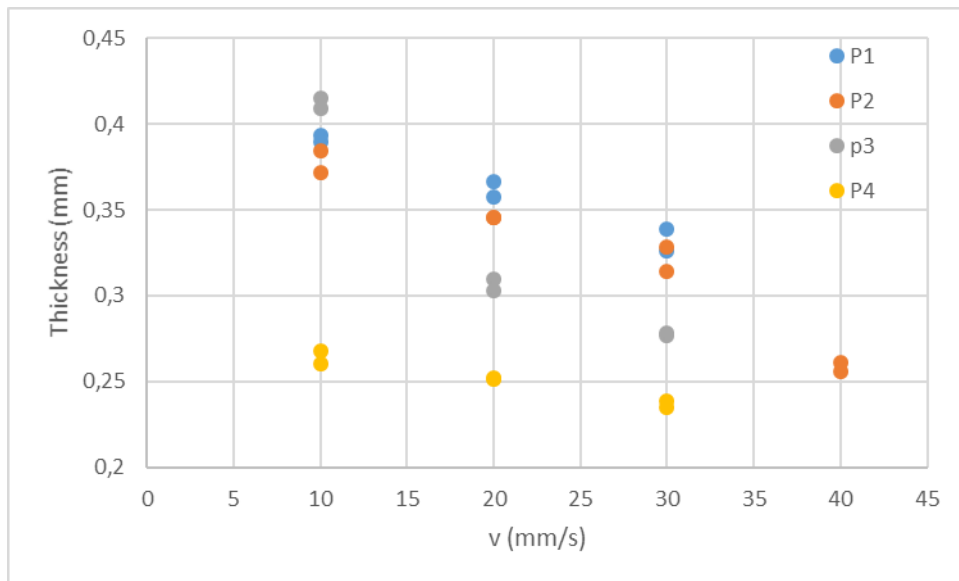


Figure 19. Thickness of the cast tapes as a function of cast velocity

The surface quality of the cast tapes can be improved via hot rolling press process. Homogeneous, smooth surfaces with almost no defects were obtained with the P2, P3 and P4 CALORIVAC tapes. At the same time, the thickness of the thin tapes is further reduced, and their green density is increased. With the tape casting and the rolling press process, the shaping is complete. The thermal treatment was thus investigated. For this project, VAC purchased a dedicated debinding furnace for the extraction of the organic additives required during shaping (Figure 20). Parallel to the development of the tape casting process, the furnace was put into operation, debugged and optimized for the debinding of CALORIVAC.

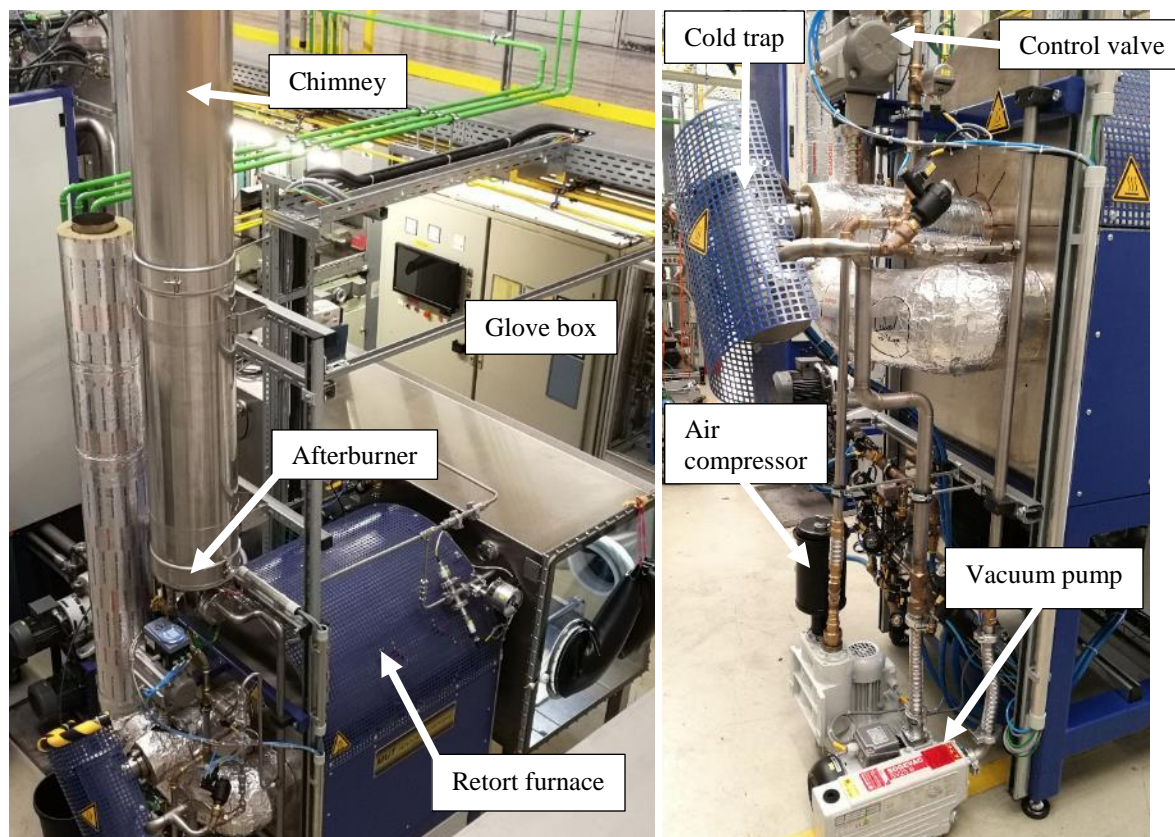


Figure 20. The debinding furnace for the heat treatment of the cast tapes. Several components are explicitly indicated

The Ni-based retort furnace was designed for heat treatment under Argon and Hydrogen up to 1120°C. For typical debinding temperatures up to 600°C it is also possible to evacuate the ~40-liter furnace volume. In this temperature range the vacuum pump in combination with a control valve allows debinding under partial vacuum. The furnace can process up to 20 kg with a good temperature homogeneity. The debinding products either condense in a cold trap or are burned in an afterburner. The Hydrogen afterburner with heating elements burns continuously and the gas-like sub-products are conducted through an exhaust chimney to the atmosphere. The furnace is coupled to an Argon-operated glove box which allows the handling of Oxygen-sensitive products such as CALORIVAC.

The green tapes were debinded below 500°C under hydrogen. The samples were sintered afterwards and then hydrogenated as indicated elsewhere [2] [3]. Figure 21 shows the tapes after sintering. As observed, the form of the tapes was preserved with minor cracks on the edges. The uppermost tape corresponds to the *P1* composition and was therefore sintered in the as cast state (not roll-pressed). A clear pigmentation on the surface is observed due to the drying process. *P2* (middle) and *P3* (down) show very good surface quality. The *P4* tape was cut into small plates (10 x 10 mm) before treatment. These plates were well preserved with no signs of cracking and with very good flatness. The density of the tapes was 7.1 g/cm³, very close to the density of the raw powder of 7.5 g/cm³.



Figure 21. The tapes after debinding and sintering. The results show that the tapes withstand the heat treatment with minor defects

Since the tapes were prepared under air, a large oxygen pick-up was expected, leading to a small magnetocaloric effect. In order to demonstrate the viability of the process from the magnetocaloric properties perspective, a *P3* slurry was cast under an inert atmosphere and later hot-roll pressed. The tape was cut into small plates, debound, sintered and hydrogenated. The obtained plates are shown in Figure 22. Some of the plates show a good flatness with almost no sign of fracture. The magnetocaloric properties were measured and are also shown in Figure 22. An adiabatic temperature change of 4.3 K at a peak temperature of 37.1°C for a field change of 1.5 T is observed. This value is comparable to the typical temperature changes of CALORIVAC-H produced by the standard powder metallurgical way.

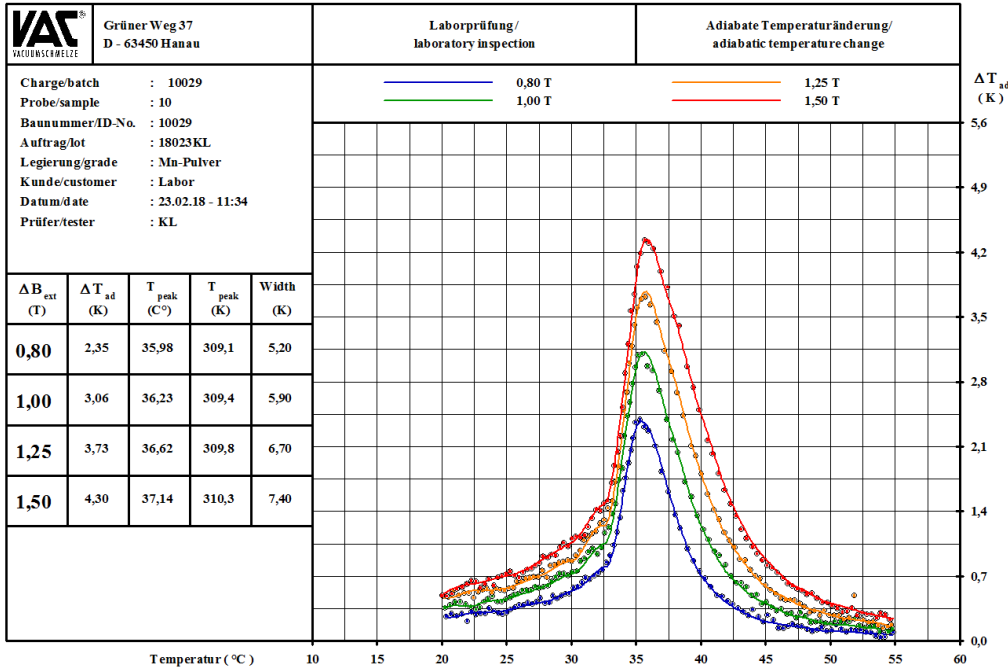
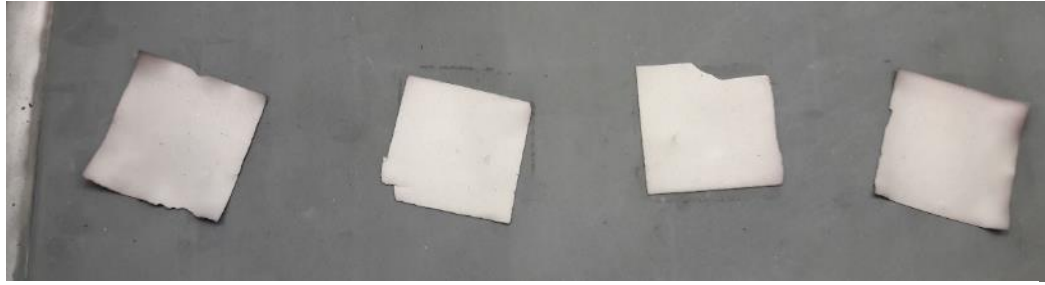


Figure 22. Sintered and hydrogenated plates of a P3 slurry cast and pressed under inert gas. The magnetocaloric properties are comparable to the standard CALORIVAC-H values

The production of thin CALORIVAC tapes with thickness below 500 μm via tape casting has been demonstrated. The combination of the tape casting and hot rolling press processes yields homogeneous tapes with good surface quality. After thermal treatment (debinding, sintering and hydrogenation), fully dense and magnetocalorically active tapes are obtained. These plates can be further optimized for their application in a solid-state magnetocaloric system.

3. COMMERCIALIZATION

This goal of the commercialization task was to investigate the challenges to commercialization of a solid-state air conditioner and identify the barriers to market entry. In December 2017, ORNL published a report that reported on the commercialization aspects of the technology [4]. A summary of the report will be recapped in the following subsections.

The report laid out a commercialization plan for solid-state magnetocaloric air-conditioners (SMC AC) that addresses key aspects of market readiness. Specifically, it:

3.1 COMPETITIVE ADVANTAGES OF THE SMC AC

The SMC AC is fundamentally different than conventional air-conditioners. It is a transformative technology that simultaneously address the needs of end-users, reduces national energy consumption, and

contributes to meeting global environmental goals. The key competitive advantages of the SMA AC can be summarized in the following points:

- **Improved System Efficiency:** the SMC AC can achieve energy saving of 25% compared to minimum efficiency vapor compression systems. This efficiency improvement qualifies it for the ENERGY STAR label.
- **No Refrigerant Required:** refrigerants are significant contributor to global warming and greenhouse gases emissions. The SMC AC does not use conventional refrigerants and replaces them with the use of magnetocaloric materials. Therefore, no direct nor indirect refrigerant emissions are associated with the use of the SMC AC.
- **Operating Cost Savings:** as direct result of its efficiency gain, the SMC AC reduces the cost of electric utility bills.
- **Peak Demand Reduction:** space cooling accounts for a large portion of peak demand in many areas of the country. Wide adoption of the SMC AC results in significant reduction of peak demand for many electric utilities nationwide due its lower energy consumption.

3.2 MARKET SEGMENT AND SIZE

Market segment investigation focused on the small room air-conditioner (RAC) market, i.e. window and through the wall air conditioners. The reason is that segment is in the same capacity as the planned SMC AC prototypes (< 20 kBtu/hr). The RACs exist in about 26 million single- and multi-family homes across the US. As shown in Figure 26, they are the most common in the northeast region of the US where the need for cooling is periodic and consumers invest less in space cooling equipment. RACs are more common in apartment buildings and mobile homes than in single-family homes.

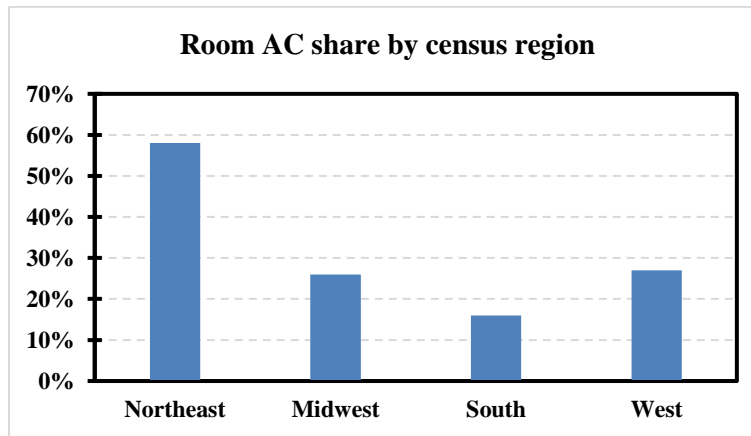


Figure 23. Room AC share of residential space cooling market by region

It is worth noting that the RAC market segment, although suitable for the SMC AC, may not be the optimal one. This market segment is driven by first cost and less amenable to adopting to new maintenance routines and requirements. Commercial size market may be more suitable to introducing the SMC AC. The commercial market is more cognizant of the life cycle cost. It also can adapt more easily to new maintenance requirements. In 2015, RAC accounted for 5% of the total AC market. The RAC segment was expected to grow from \$1.345B to \$1.815B by 2019 and to \$2.225B by 2024. The annual shipment of the RAC was estimated to be almost 7M units.

3.3 MARKET POTENTIAL

An analysis was performed to forecast the maximum market penetration of the SMC AC as function of its payback period. The baseline cost against which the payback period of the SMC AC is calculated is the cost of RAC. The average total installed cost of RAC was estimated by calculating the weighted average retail price and weighted average installation cost of all relevant product categories in the RAC size as listed in the DOE Technical Support Document for Residential AC [5]. The baseline annual cost of operation was calculated by estimating the weighted average efficiency and weighted average runtime hours of all relevant product categories. The baseline total installed cost and annual operation cost are summarized in Table 4.

Table 4. Baseline costs used in the calculation of SMC AC payback period

Weighted average retail price	\$272
Weighted average installation cost	\$104
Weighted average total installed cost	\$376
Weighted average unit EER	11.3
Weighted average unit size (Btu/h)	8,055
Average operating time (h/yr)	750
Weighted average electricity consumption (kWh/y)	534
Weighted average annual operation cost	\$67

The payback period of the SMC AC was then calculated for different hypothetical scenarios of installation cost premium and operational cost savings. Table 5 summarizes the scenarios and the results.

Table 5. SMC AC payback period scenarios

Simple payback period		Total installed cost premium		
		\$50	\$100	\$200
Operating cost saving	5%	15	30	60
	15%	5	10	20
	25%	3	6	12

The method that is suggested by the Building Technologies Office of the US Department of Energy is used to forecast the market penetration of the SMC AC based on its payback [6]. The results are shown in Table 6 for only the 3- and 5- year payback periods. Longer payback periods are deemed too long for residential market, and optimally, payback periods for shorter life period appliances such as RAC are in the range of 1 to 3 years.

Table 6. Time trend of maximum penetration after commercial viability

	1 year after commercial viability	5 years after commercial viability	Ultimate adoption
3-year payback	0 – 5%	2 – 7%	13 – 18%
5-year payback	0 – 3%	1 – 5%	8 – 12%

The baseline cost and the payback period calculations are then used to calculate pricing guidance for the SMC AC based on payback and operation cost saving (directly correlated to energy efficiency improvement over the baseline). The results are presented in Table 7.

Table 7. SMC AC price point guidance

Payback period (years)	Operation cost saving		Max retail price
1	5%	\$3.35	\$275.71
	15%	\$10.05	\$282.41
	25%	\$16.75	\$289.11
2	5%	\$3.35	\$279.06
	15%	\$10.05	\$292.46
	25%	\$16.75	\$305.86
3	5%	\$3.35	\$282.41
	15%	\$10.05	\$302.51
	25%	\$16.75	\$322.61
4	5%	\$3.35	\$285.76
	15%	\$10.05	\$312.56
	25%	\$16.75	\$339.36
5	5%	\$3.35	\$289.11
	15%	\$10.05	\$322.61
	25%	\$16.75	\$356.11

In conclusion, for commercial viability the SMC AC should cost ~\$37 per kBtu/hr of rated cooling capacity.

3.4 STEPS TOWARD SUCCESSFUL MARKET ENTRY

The first step toward successful market entry is to identify the value chain differences between the SMC AC and the baseline technology it is competing against, RAC. The differences emerge in all segments of the value chain. Table 8 lists the differences categorized by value chain segment, and the magnitude of the anticipated difference.

Table 8. Anticipated cost differences between SMC AC and conventional vapor compression RAC

	COST/COMPLEXITY INFLUENCERS	ANTICIPATED DIFFERENCE
Raw Material Cultivation / Processing	<ul style="list-style-type: none"> • Difference in cost to acquire/prepare/assemble/package raw material or component? 	Significant additional cost
Purchase of Supplies, Materials, Incoming Shipping	<ul style="list-style-type: none"> • Difference in shipping cost, point of origin? • Difference in mode of transportation? • Difference in materials handling/storage methods? 	Moderate cost saving

Manufacturing and Operations	<ul style="list-style-type: none"> • Assuming economies of scale, difference in manufacturing cost per appliance? • Capital costs of new/repurposed production line (e.g., new machine tools, downtime)? • Difference in packaging process? 	Moderate additional cost
Outgoing Shipping and Logistics	<ul style="list-style-type: none"> • Difference in shipping cost, destination? • Difference in mode of transportation? • Difference in materials handling/storage methods? 	None
Marketing and Retail Sales	<ul style="list-style-type: none"> • Difference in media/branding/outreach investments required? • Difference in retail price? • Applicable purchase discounts (e.g., ENERGY STAR tax credits)? 	Moderate additional cost
Installation	<ul style="list-style-type: none"> • Difference in technique? • Difference in required tools, materials? • Difference in required labor? 	None
Product End Use	<ul style="list-style-type: none"> • Difference in operating cost? • Available utility incentives? 	Moderate cost saving
After-Sale Maintenance, Repair and Recycle	<ul style="list-style-type: none"> • Difference in diagnostic techniques? • Difference in required labor? • Difference in replacement parts/fluids, costs? • Difference in time/cost required to properly recycle components (if applicable)? 	Moderate additional cost

Those differences give rise to obstacles to market entry of the SMC AC. In the following, obstacles will be summarized for each value chain segment:

- **Upstream suppliers:** the supply chain of the rare earth metals that are used in the SMC AC has been known to be volatile due to rising demand, political factors and lack of competition. For example, in 2011 the price of dysprosium increased by almost ten folds within only few months.
- **Manufacturers:** the manufacturing of the SMC AC is quite different to that of a conventional RAC. New production lines will need to be built, or existing ones will need to be retooled. Either option brings about significant capital cost. The SMC AC will need to comply with design constraints, such as dimensions and weight, that were originally set mainly for RAC. Noise emissions and reliability will need to not exceed those of the RACs. Designers and manufacturers of the SMC AC will need creative solution to satisfy those constraints.
- **Contractors/installer/service:** the SMC AC may require different installation and maintenance techniques that are not familiar to the existing HVAC&R workforce. Training materials will need to be developed.

- **End-users:** consumer acceptance is typically a challenge for new appliances. Efforts will need to be concerted to educate end-users on the benefits of the SMC AC relative to the RAC, and to address their hesitation.

A group of industry experts was polled to assess the barriers to market entry of the SMC AC by assigning values (ranging from 1 to 10) to:

- A barrier's potential impact on market success (1= very small and 10 = very large)
- The degree of difficulty associated with overcoming the barrier (1= very simple and 10 = very difficult)

The higher the score of impact and difficulty to overcome, the higher the priority that should be given to addressing the barrier. The assessment of the experts is plotted in Figure 24. The consensus was that the design constraints were the highest priority. Design constraints refer to the production of the SMC AC within the weight, dimensions, noise and reliability limits that are already set by the incumbent technology, RAC.

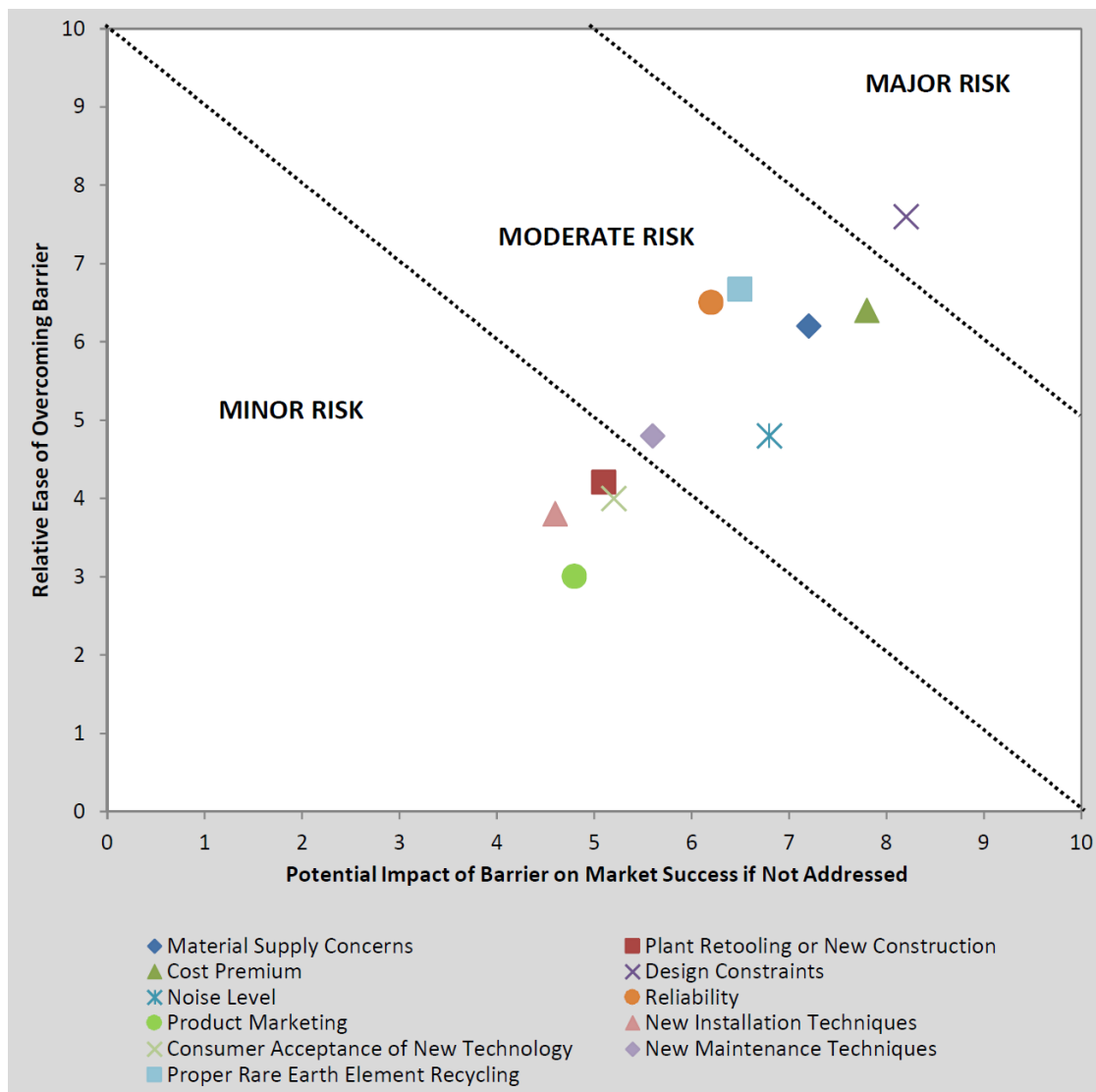


Figure 24. Industry experts' assessment of the barriers impact and ease of overcoming

4. MODELING AND PROTOTYPING

To build a solid-state prototype, the MCM manufacturing method would have had to be finalized first. The project team decided to build a proof of concept prototype using a liquid metal heat transfer medium while the MCM manufacturing method is still being developed. Therefore, two different physics-based analytical models were developed: one that models liquid heat transfer medium [7] and one that models metallic one [8]. Brief recap of each model and its main findings are presented in the following subsections.

4.1 SOLID STATE MODEL

The AMR was modeled as a copper sheet sandwiched between two MCM plates Figure 25. The gaps between the sheet and the MCM was modeled as filled with low viscosity thermal grease. It was assumed that an external pressure was applied on both sides of the MCM blocks to maintain good contact between the MCM and the copper plate. The plates and the MCM were assumed to have the same surface roughness.

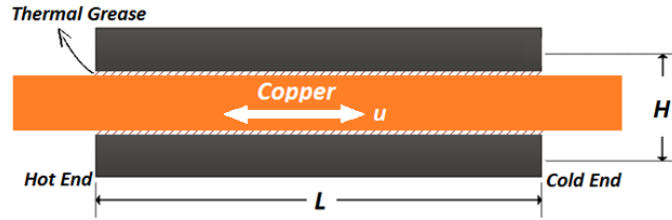


Figure 25. Representation of solid-state AMR [8].

The problem was modeled as one-dimensional. The model was discretized in both time and space and solved numerically. Sensitivity analysis was performed to characterize the effect of the apparent applied pressure, the effective surface roughness, and the thermal conductivity of the thermal grease on the cooling capacity and the COP. The levels of those three parameters are listed in Table 9. Fifteen simulations were performed for different combinations of the three parameters. The combinations were determined by using Box-Behnken design of experiment.

Table 9. Parameter levels for design of experiment

Parameter	Levels
Apparent pressure (P), MPa	5, 12.5, 20
Effective surface roughness (σ), μm	0.2, 4.9, 9.6
Grease thermal conductivity (K_g), W/m-K	0.2, 0.45, 0.7

The cooling capacity and COP results of the fifteen simulations were fit to quadratic response surfaces. The coefficients of the fits are shown in Figure 26. The coefficients show that the surface roughness has the largest effect on both the capacity and the COP. The apparent pressure was the second most significant parameter. Thermal conductivity of grease had the least impact among the three parameters. Due to their non-linear effects, the correlation between either of the pressure or the roughness to both capacity and COP is not monotonically positive. At certain roughness (or pressure), increasing the pressure (or roughness) may reduce both the capacity and COP. The optimal roughness and pressure combination were found to be $0.2 \mu\text{m}$ and 15 MPa.

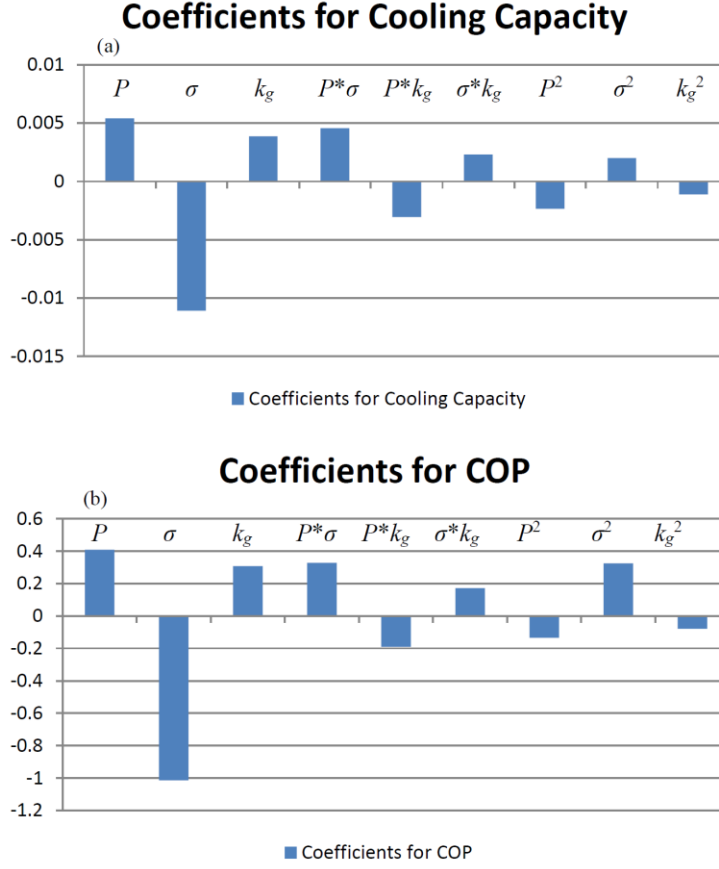


Figure 26. Response surface fitting coefficients [8].

The performance of the solid-state AMR was compared to the performance of liquid-based AMR for operational frequency of 0.5 Hz and 5 Hz. The solid-state AMR simulations were performed using pressure of 15 MPa, roughness of 0.2 μm and grease thermal conductivity of 0.7 W/m-K. The comparison of the capacity and COP of both systems as function of utilization are shown in Figure 27.

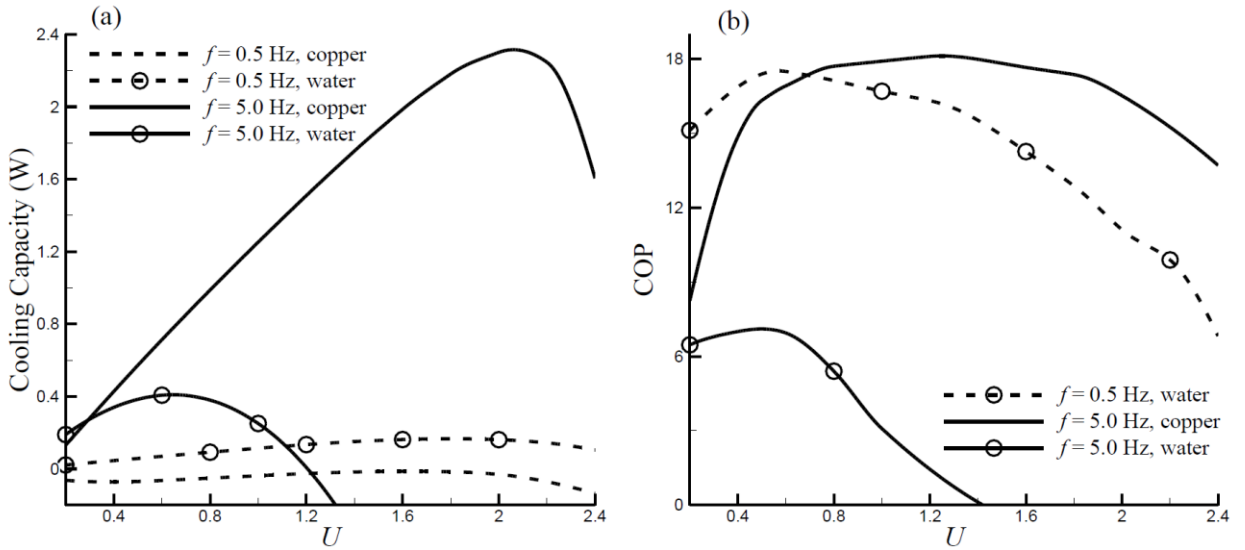


Figure 27. Capacity and COP comparison of solid-state and liquid-based AMR [8].

Figure 27 clearly shows the effect of the thermal conductivity of the heat transfer medium. At 0.5 Hz, the metallic heat medium does not produce any cooling capacity. Heat is dissipated axially along the metallic sheet before it can be dissipated to the hot end sink. At 5 Hz, the liquid heat transfer medium initially produces some cooling capacity. As the flow rate of the liquid increases, the capacity drops and eventually no capacity is produced. This is because the residence time is too short for heat to be transferred between the MCM and the liquid. At the same frequency, the metallic heat transfer medium however produces one order of magnitude higher capacity.

4.2 LIQUID-BASED AMR MODEL

A model was developed to simulate the performance of multi-layer packed-particle bed. Each layer is an MCM of different curie temperature. The highest curie temperature MCM is located at the hot end and the lowest curie temperature MCM is located at the cold end. The in-between layers are ordered in descending curie temperature. The liquid heat transfer medium is pumped through the particle bed. The problem was modeled as one-dimensional. The model was discretized in time and space and solved numerically.

A 16-layer AMR was simulated for different utilization values. Figure 28 shows the cooling capacity and the COP at different operational frequencies. The maximum cooling capacity monotonically increased as the frequency increased. At the same frequency, the capacity increased as the utilization increased up to certain value after which the capacity decreased as the utilization increased. The maximum COP showed different behavior. It did not monotonically increase as the frequency increased. The maximum COP was obtained at frequency of 0.1 Hz.

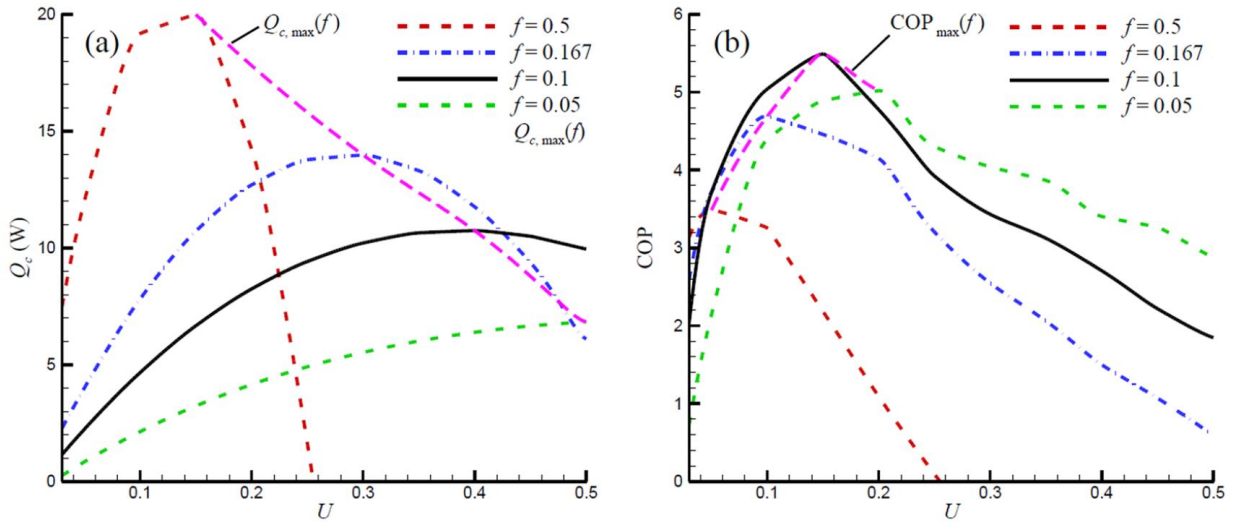


Figure 28. Cooling capacity and COP for 16-layer liquid-based AMR as function of utilization for different frequencies [7].

Simulations were then performed for AMR's with different number of layers at frequency of 0.1 Hz. Figure 29 shows the results. The 10-layer AMR produced the highest capacity while the 16-layer one had the highest COP.

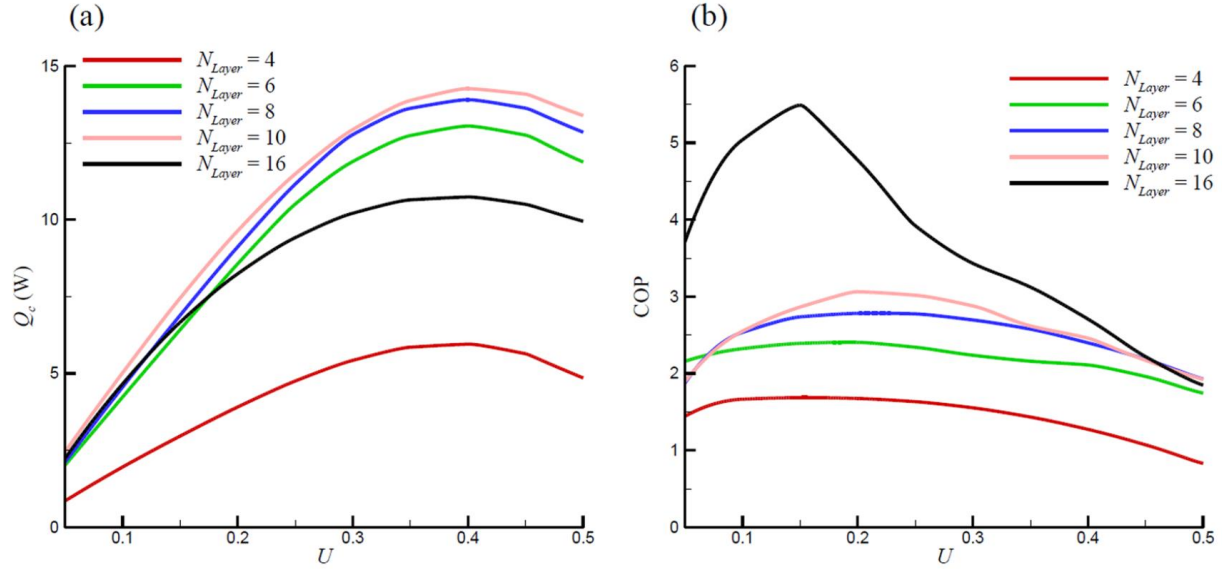


Figure 29. Effect of number of layers of liquid-based AMR on the cooling capacity and the COP [7].

An analysis was done to investigate the effect of the length of each layer in the AMR on the COP and capacity. It was found that, for the same AMR length, cooling capacity is increased if the layer at the cold end is longer than the rest. However, this also reduces COP.

4.3 PROTOTYPE DEVELOPMENT

Two prototypes were developed under this project, both were meant to use liquid metal to prove the concept. The first used a C-shaped fixed permanent magnets and reciprocating regenerator. The second used a fixed tubular regenerator and a rotating Halbach array of permanent magnets.

4.4 C-SHAPED PROTOTYPE

In this prototype, the movement of the regenerators and the movement of the pumping system were mechanically couples. Two regenerator tubes were mounted on two opposite sides of a tray, one on each side. A cam drove the tray in reciprocating motion to move the regenerator tubes in and out of the magnetic field of the magnets Figure 30. The magnets were made of Alnico and were designed and supplied by a large magnets and magnetic systems vendor to have a maximum field of 1.5 Tesla . The profile of the cam was manufactured to give near-square wave movement, with sharp rise and fall and long dwelling.



Figure 30. The C-shaped prototype showing the regenerators cam relative to the placement of the magnet. The cam profile is shown in the upper left corner. One magnet is shown in the lower right corner.

On the same shaft of the regenerators cam, another cam is mounted to push/pull plungers of two stainless steel syringes to pump the heat transfer fluid (Figure 31). The plungers move sinusoidally in tandem; when one plunger is being pushed to pump, the other is being pulled to suction.

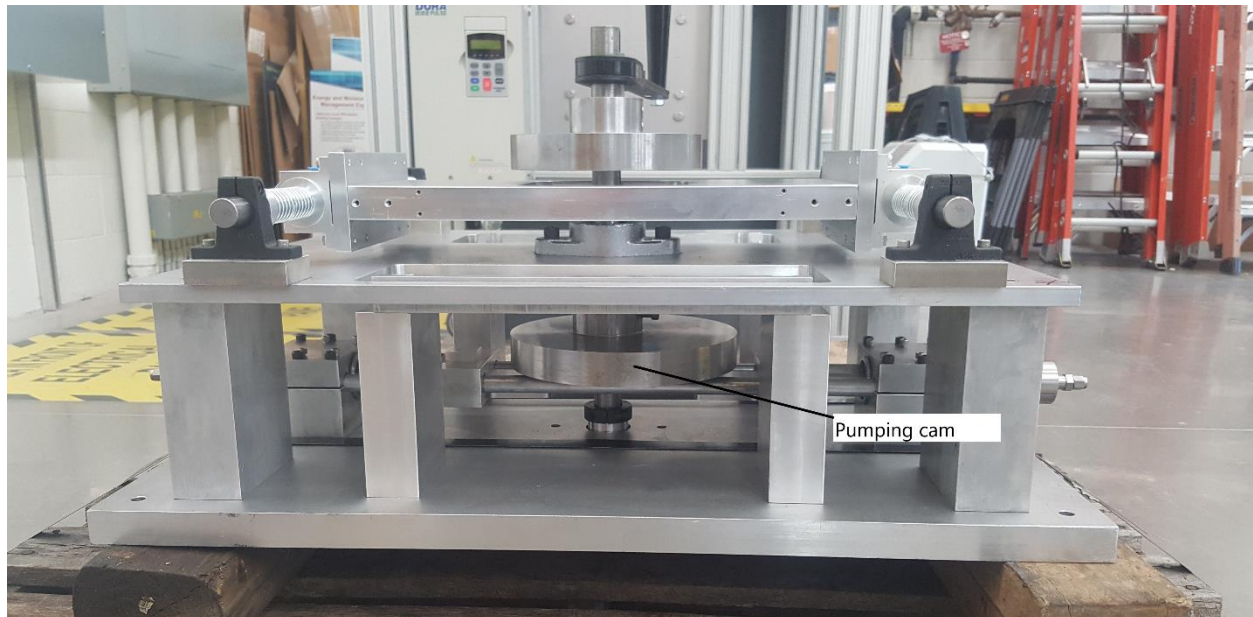


Figure 31. Location of the pumping cam

The regenerator tubes had rectangular cross section. Special caps were manufactured to seal the ends of the regenerator tubes while providing a flow path for the heat transfer fluid and holes to mount the caps to the regenerators tray Figure 32.

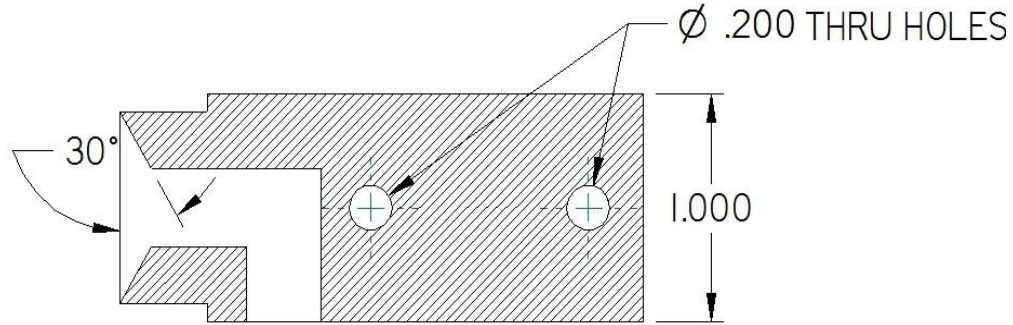


Figure 32. Regenerator end caps. the thru holes are for mounting the regenerator tubes to the tray.

Figure 33 shows the assembled prototype with tube-in-tube heat exchangers and check valves.

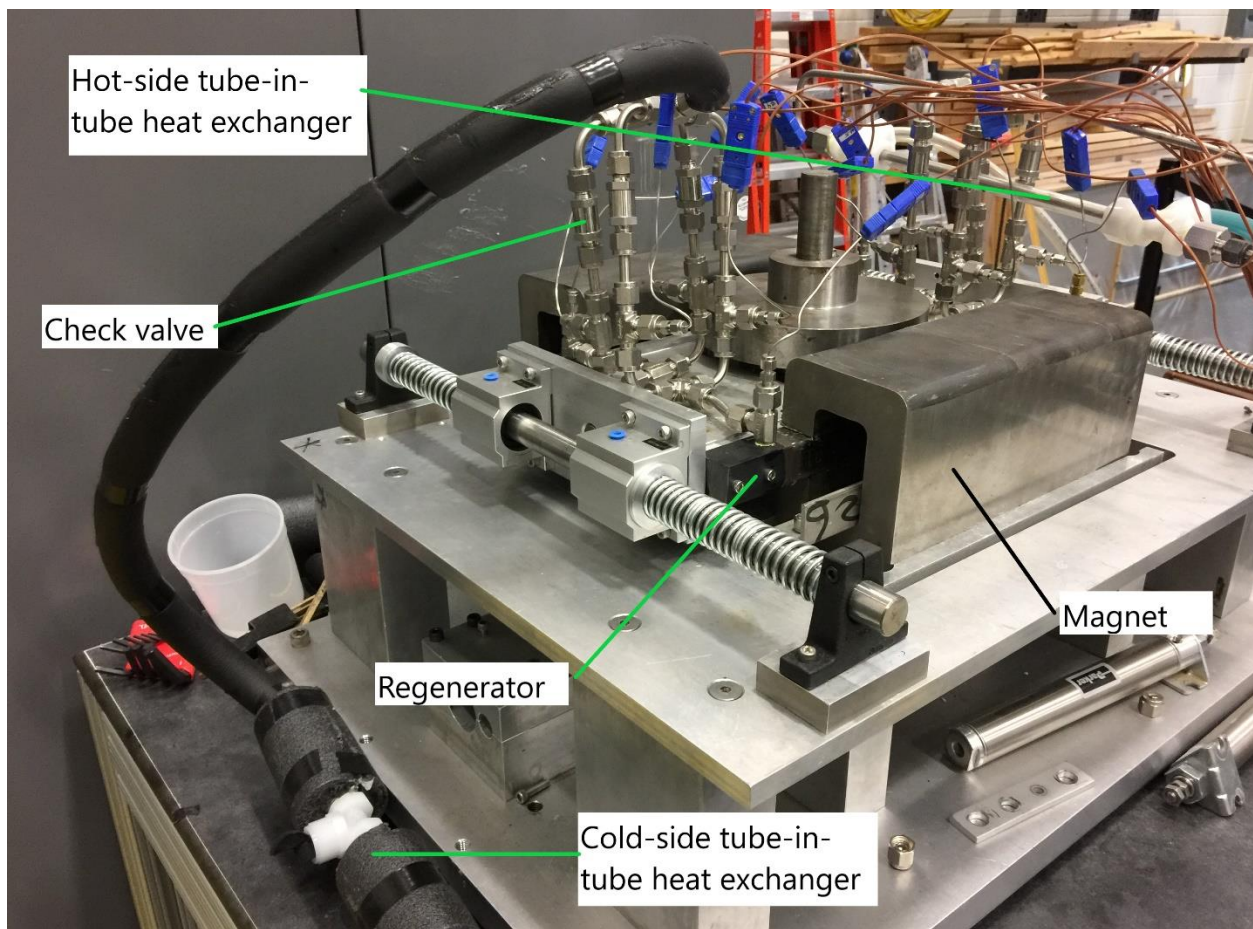


Figure 33. Assembled prototype

The prototype was commissioned using water as heat transfer fluid to check the operation before switching to Galinstan. The prototype was run at no-load at frequencies of up to 1 Hz but no temperature difference could be achieved. It was decided to switch the pumping of the heat transfer fluid (water) to external pumping system to adjust the flow rate in case that was the reason for achieving zero temperature span at no-load. The external pumping system consisted of linear actuator driving two hydraulic cylinders in tandem Figure 34.

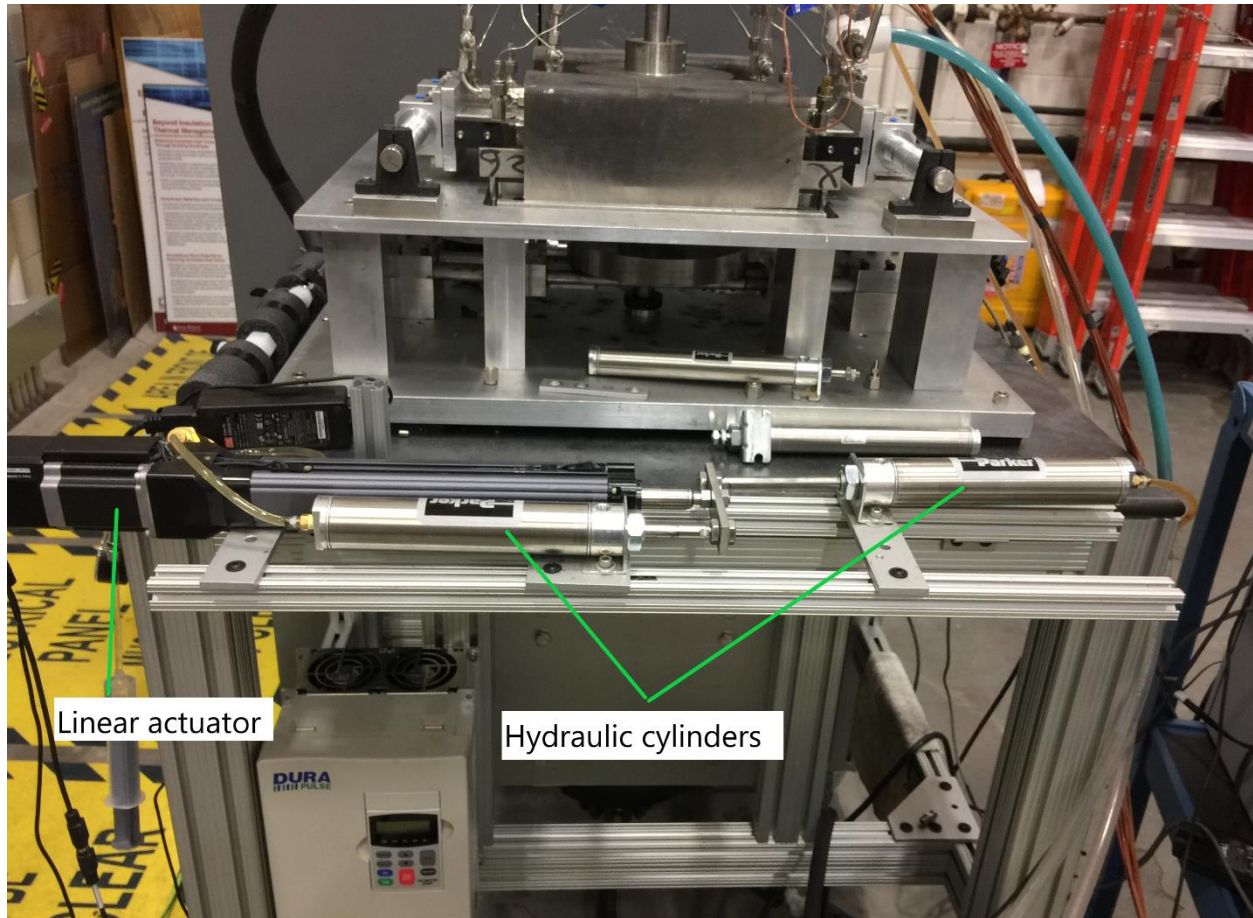


Figure 34. External pumping system

The prototype still produced no temperature span at no-load. Eventually, the magnetic field strength in the air gap of the magnets was measured. It turned out that the field was only 0.3 T. No resolution could be reached with the vendor and no other vendor could provide quote for 1.5 T within the existing envelope. It was decided to switch to a Halbach prototype.

4.5 HALBACH PROTOTYPE

Figure 35 shows the Halbach magnet array and its rotating mechanism. The array is rotated using a 1:3 pulley system which is driven by a servo motor for precise angular control.

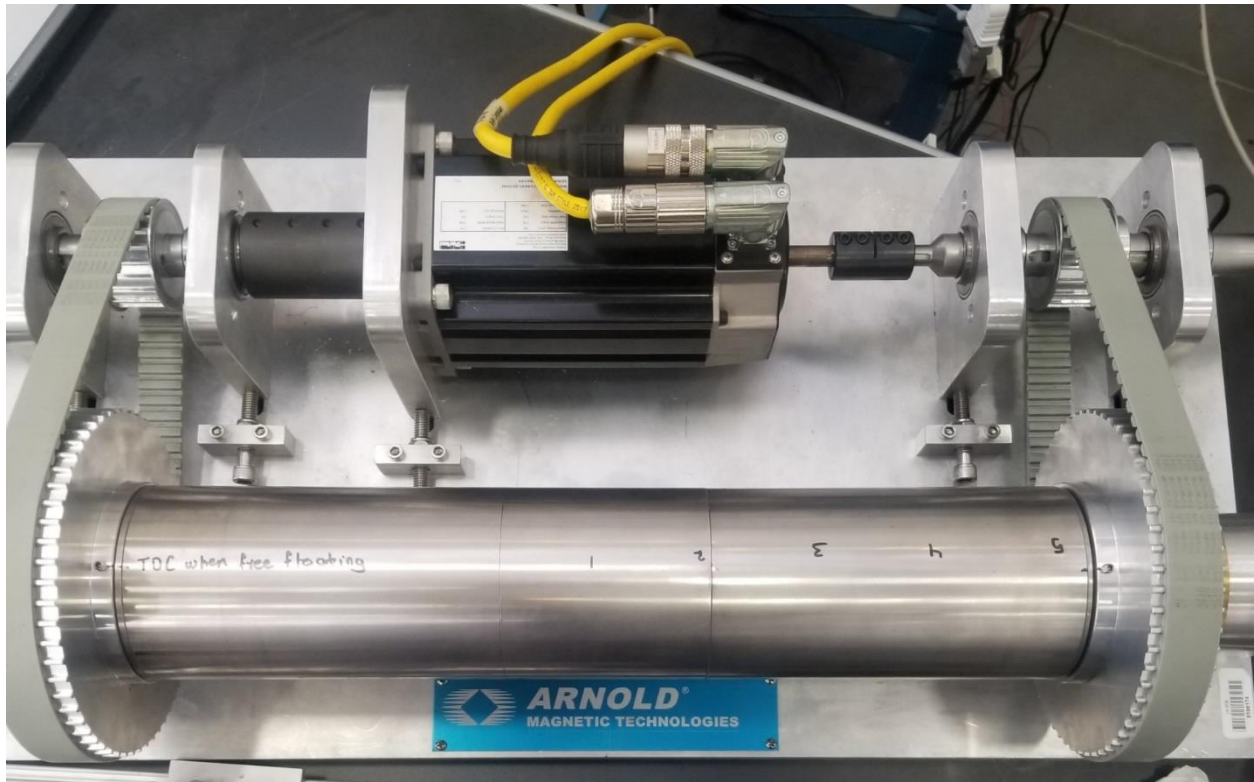


Figure 35. The Halbach magnet array

The Halbach array was design to provide a uniform maximum magnetic field of 1.5 T over 12 inches in the middle of the array, and a minimum field of less than 0.04 T. The field was measured along the length of the array in the laboratory at different rotating angles. The measurements were taken at 0, 1.94, 4.21, 6.44 and 8.69 inches from the middle point of the array, point 1 through 5 respectively. Reference angle (0° position) is at the minimum field angle (freely resting position of the array). Figure 36 shows the field measurements. Over the 12 inches in the middle of the array, the field was uniform with maximum strength of 1.3 T and minimum strength of 0.4 T.

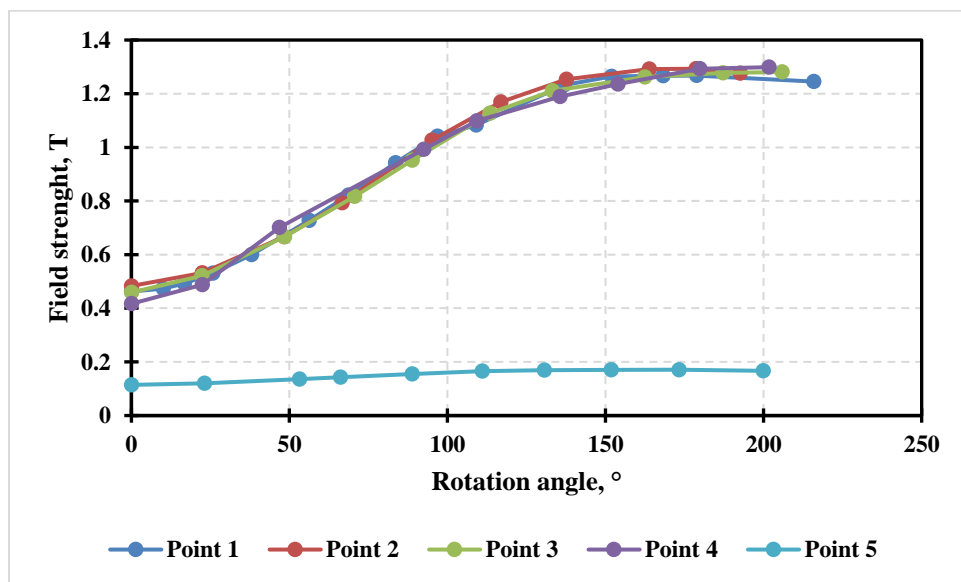


Figure 36. Magnetic field strength at points 1 through 5 against rotation angle of the magnet array

Figure 37 shows Halbach array after plumbed to the regenerator tube and an external pumping system.

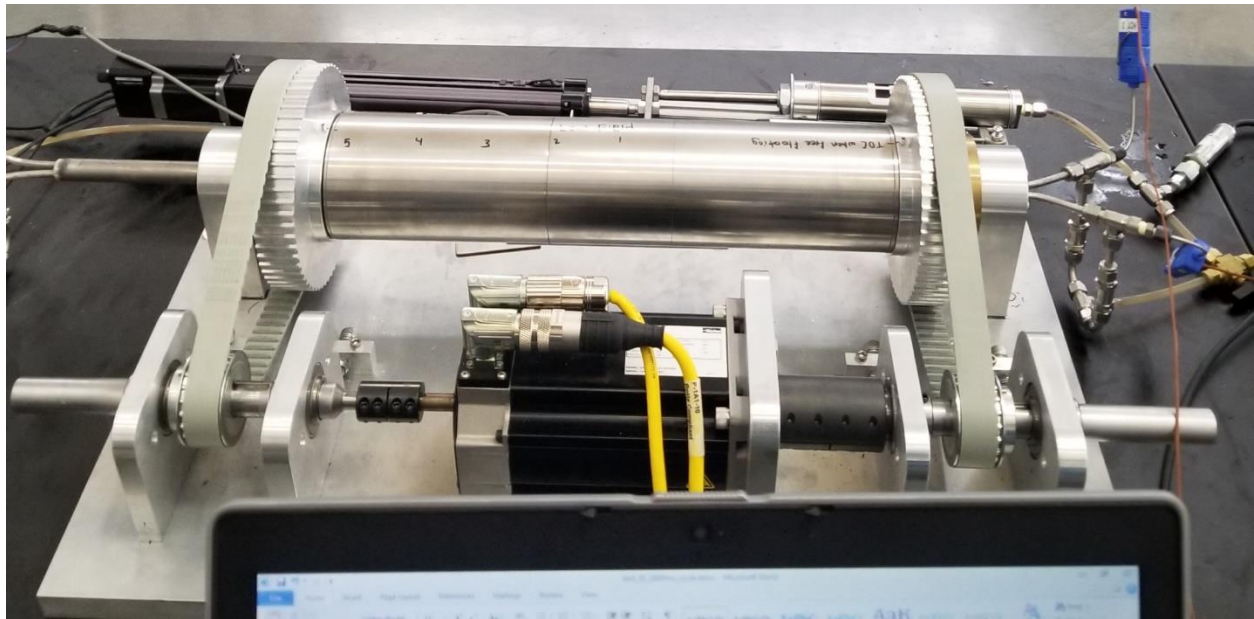


Figure 37. The assembles prototype showing the regenerator tube sticking out of the left end of the Halbach array

The prototype was run with water as heat transfer fluid at no-load to verify its operation. A 27°K no-load temperature span was achieved in 200 minutes at operating frequency of 0.6 Hz (Figure 38).

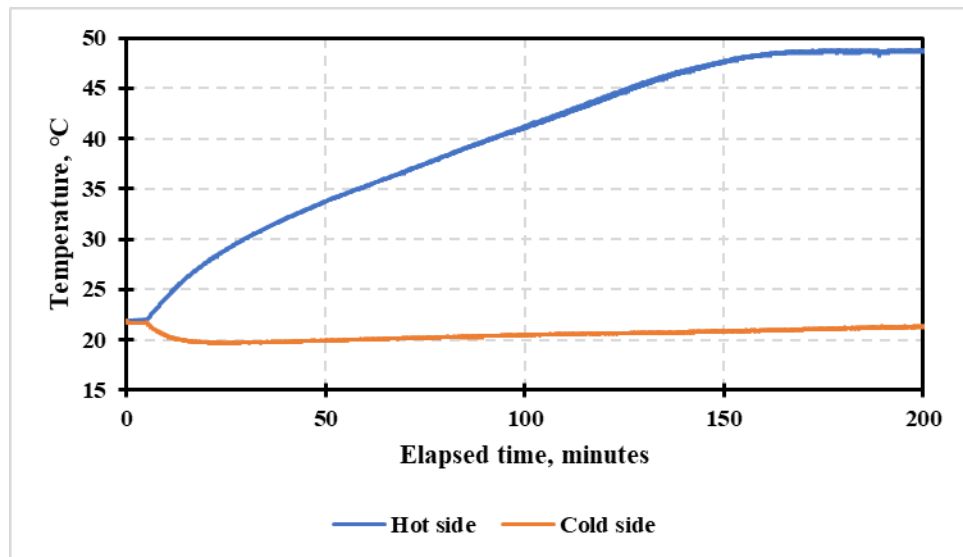


Figure 38. No-load temperature span. Operating frequency is 0.6 Hz.

The heat transfer fluid was then changed to Galinstan. The prototype was first run at 2 Hz, hot end heat sink temperature of 35°C and cold-end sink temperature of 27°C. The prototype produced cooling capacity of 34 Watts at COP of 0.4. Quickly after commissioning the prototype with Galinstan, we started to notice that the pressure of the whole system started to continuously increase. The prototype was stopped, but the pressure kept increasing even with no energy input to the system (no movement).

It was suspected that Galinstan chemically reacted with the MCM, and the release of the products of that reacting caused the pressure increase. This hypothesis was confirmed through preliminary XRD characterization of the MCM before and after exposure to Galinstan. Further testing was underway at the time of writing this report. The results will be published at a later time after all characterization work has been completed.

5. REFERENCES

- [1] A. M. Momen, O. Abdelazize and E. A. Vineyard, "Magnetocaloric refrigeration using fully solid state working medium". United States of America Patent US10443905B2, 15 October 2019.
- [2] M. Katter, Z. Zellmann and A. Barcza, "SINTERING BEHAVIOUR AND THERMALLY INDUCED DECOMPOSITION AND RECOMBINATION (TDR) PROCESS OF $\text{LaFe}_{13-x}\text{-yCo}_x\text{Si}_y$ ALLOYS," in *Proceedings of the 4th International Conference on Magnetic Refrigeration at Room Temperature*, Baotou, China, 2010.
- [3] A. Fujita, S. Fujieda, Y. Hasegawa and K. Fukamichi, "Itinerant-electron metamagnetic transition and large magnetocaloric effects in $\text{La}(\text{Fe}_x\text{Si}_{1-x})_{13}$ compounds and their hydrides," *Phys. Rev. B*, vol. 67, no. 10, p. 104416, 2003.
- [4] K. Sikes, J. Blackburn, O. Abdelaziz, A. Mehdizadeh Momen and A. Abu-Heiba, "Bringing Solid-State Magnetocaloric Cooling to the Market: A Commercialization Plan," Office of Scientific and Technical Information, U.S. Department of Energy, 2017.
- [5] US Department of Energy, "2011-04 Technical Support Document: Energy Efficiency Program for Consumer Products and Commercial and Industrial Equipment; Residential Clothes Dryers and Room Air Conditioners," Energy Efficiency and Renewable Energy Office, U.S. Department of Energy, Washington D.C., 2011.
- [6] Building Technologies Program, "Guide for Evaluation of Energy Savings Potential," Office of Energy Efficiency and Renewable Energy, U.S. Department of Energy, 2005.
- [7] M. Zhang, O. Abdelaziz, M. Ayyoub Mehdizadeh and A. Abu-Heiba, "A numerical analysis of a magnetocaloric refrigerator with a 16-layer regenerator," *Scientific Reports*, vol. 7, 2017.
- [8] M. Zhang, A. M. Momen and O. Abdelaziz, "Preliminary Analysis of a Fully Solid State Magnetocaloric Refrigeration," in *16th International Refrigeration and Air Conditioning Conference*, Purdue, 2016.
- [9] T. F. Petersen, K. Engelbrecht, C. R. H. Bahl, B. Elmegaard, N. Pryds and A. Smith, "Comparison between a 1D and a 2D numerical model of an active magnetic regenerative refrigerator," *Journal of Physics D: Applied Physics*, vol. 41, 2008.